BRNO UNIVERSITY OF TECHNOLOGY
VYSOKÉ UČENÍ TECHNICKÉ V BRNĚ

FACULTY OF MECHANICAL ENGINEERING
FAKULTA STROJNÍHO INŽENÝRSTVÍ

INSTITUTE OF PHYSICAL ENGINEERING
ÚSTAV FYZIKÁLNÍHO INŽENÝRSTVÍ

CHARACTERIZATION OF ELECTRONIC PROPERTIES OF NANOWIRES FOR ELECTROCHEMISTRY
CHARAKTERIZACE ELEKTRONICKÝCH VLASTNOSTÍ NANODRÁTŮ PRO ELEKTROCHEMII

MASTER'S THESIS
DIPLOMOVÁ PRÁCE

AUTHOR — **Bc. Martin Kovařík**
AUTOR PRÁCE

SUPERVISOR — **doc. Ing. Miroslav Kolíbal, Ph.D.**
VEDOUCÍ PRÁCE

BRNO 2019

VYSOKÉ UČENÍ TECHNICKÉ V BRNĚ
FAKULTA STROJNÍHO INŽENÝRSTVÍ

Zadání diplomové práce

Ústav:	Ústav fyzikálního inženýrství
Student:	**Bc. Martin Kovařík**
Studijní program:	Aplikované vědy v inženýrství
Studijní obor:	Fyzikální inženýrství a nanotechnologie
Vedoucí práce:	**doc. Ing. Miroslav Kolíbal, Ph.D.**
Akademický rok:	2018/19

Ředitel ústavu Vám v souladu se zákonem č.111/1998 o vysokých školách a se Studijním a zkušebním řádem VUT v Brně určuje následující téma diplomové práce:

Charakterizace elektronických vlastností nanodrátů pro elektrochemii

Stručná charakteristika problematiky úkolu:

Plazmonově zesílená elektrochemie je v současnosti intenzivně studovaným oborem. Naráží však často na nedostatečně prozkoumané elektronické vlastnosti použitých elektrod. Student se zaměří na analýzu elektronických vlastností kvazi–jednorozměrných objektů pomocí UPS a KPFM.

Cíle diplomové práce:

1. Navrhněte metodologii měření elektronických vlastností nanodrátů a pokuste se taková měření realizovat.
2. Navrhněte metodologii měření Kelvinovou sondou za současného osvitu externím zdrojem světla.

Seznam doporučené literatury:

WALLS, J. M. Methods of surface analysis: Techniques and Applications, ed. J. M. Walls, Cambridge University Press, 1989. ISBN 0-521-38690-X.

LEDINSKÝ, M., FEJFAR, A., VETUSHKA, A., STUCHLÍK, J., REZEK, B. and KOČKA, J. Local photoconductivity of microcrystalline silicon thin films measured by conductive atomic force microscopy. Physica status solidi (RRL) - Rapid Research Letters. 2011, 5(10-11), 373-375.

Termín odevzdání diplomové práce je stanoven časovým plánem akademického roku 2018/19

V Brně, dne

L. S.

prof. RNDr. Tomáš Šikola, CSc. ředitel ústavu	doc. Ing. Jaroslav Katolický, Ph.D. děkan fakulty

Abstrakt
Elektrochemické metody nacházejí využití v mnoha aplikacích (např. senzorice, skladování el. energie nebo katalýze). Jejich nespornou výhodou je nízká finanční náročnost na přístrojové vybavení. Abychom lépe porozuměli procesům probíhajícím na elektrodách, je dobré znát elektronickou pásovou strukturu materiálu elektrody. Úkolem této práce je vyhodnotit výstupní práci a pozici hrany valenčního pásu nových materiálů pro elektrody, konkrétně cínem dopovaného oxidu india pokrytého nanotrubicemi sulfidu wolframičitého. Ultrafialová fotoelektronová spektroskopie a Kelvinova silová mikroskopie jsou metody použité pro tuto analýzu. Zvláštní důraz je kladen na přípravu vzorků elektrod pro měření, aby nedošlo k nesprávné interpretaci výsledků vlivem vnějších efektů jako je např. kontaminace nebo modifikace povrchu.

Summary
Electrochemical methods are widely used in many applications (e.g. sensing, energy storage or catalysis) with the advantage of their inexpensive instrumentation. In order to understand redox processes taking place at electrodes, the knowledge of electronic band structure of the electrode materials is very valuable. This thesis focuses on the analysis of work function and valence band edge position of novel electrode materials, in particular indium tin oxide decorated with tungsten disulfide nanotubes. Ultraviolet Photoelectron Spectroscopy and Kelvin Probe Force Microscopy are used to measure those characteristics. A special emphasis is put on the electrode sample preparation to avoid misinterpretation of the results due to adventitious effects (e.g. contamination or surface modification).

Klíčová slova
Ultrafialová fotoelektronová spektroskopie, UPS, Kelvinova silová mikroskopie, KPFM, nanodráty, nanotrubice, sulfid wolframičitý, WS2, ITO, elektrochemie

Keywords
Ultraviolet Photoelectron Spectroscopy, UPS, Kelvin probe force microscopy, KPFM, nanowires, nanotubes, tungsten disulfide, WS2, indium tin oxide, ITO, electrochemistry

KOVAŘÍK, M. *Charakterizace elektronických vlastností nanodrátů pro elektrochemii.* Brno University of Technology, Faculty of Mechanical Engineering, 2019. 60 p. Supervisor Ing. Miroslav Kolíbal, Ph.D.

I hereby declare that this thesis is my original work, written under the guidance of the thesis supervisor doc. Ing. Miroslav Kolíbal, Ph.D. I also declare that all the information obtained from technical literature and other sources is properly cited and all the sources are listed at the end of the thesis.

Martin Kovařík

In the first place, I would like to thank my supervisor doc. Ing. Miroslav Kolíbal, Ph.D. for his professional guidance and thorough proof reading of the thesis.

I am also very grateful to Ing. Josef Polčák, Ph.D. for his assistance and advice related to the XPS and UPS measurements. I would also like to thank Ing. Martin Konečný for assisting with KPFM measurements.

Last but not least, special gratitude belongs also to my fianceé Sabina for her patience and support.

Financial support from the Thermo Fisher Scientific is gratefully acknowledged.

Part of the work was carried out with the support of CEITEC Nano Research Infrastructure (ID LM2015041, MEYS CR, 2016–2019), CEITEC Brno University of Technology

Martin Kovařík

Contents

Introduction

In many applications such as sensing, energy storage or catalysis, electrochemical methods are often utilized. The biggest advantage of electrochemical methods is that usually inexpensive and simple instrumentation is needed. To achieve improved performance of devices based on electrochemistry, novel electrode materials are often studied.

One of the approaches how to improve the performace of such electrochemical devices (e.g. sensor sensitivity or catalysis rate) is the use of 1D nanostructures [1, 2]. This is mainly due to the fact that 1D nanostructures such as nanowires and nanotubes provide high surface to volume ratio and often different properties than their bulk counterparts. Also, with the use of additional metal nanoparticles, plasmon enhancement may be used for additional improvements of the electrochemical methods [3].

In order to understand the processes taking place at the electrodes, the study of their electronic properties is unavoidable. Mostly the knowledge of the electronic band structure of the electrode materials helps to predict and explain processes taking place at electrodes (i.e. when oxidation or reduction occurs or when the charge transfer is possible).

A common technique used for examining the band structure is an Ultraviolet Photoelectron Spectroscopy (UPS), which is based on the photoelectric effect. UPS can be used to determine the work function and the valence band position with respect to the Fermi level. Its advantage is that it is an absolute technique and measures the characteristics directly. However, its ultimate surface sensitivity might be also a disadvantage, since the potential surface contamination might significantly affect the measurements' outcomes. Another method used in this work to study the work function is the Kelvin Probe Force Microscopy (KPFM). This technique is a relative one so another reference work function has to be known.

The main goal of this thesis is to follow the study of indium tin oxide (ITO) electrodes covered with tungsten disulfide nanotubes (WS_2 NTs) conducted by Ing. Filip Ligmajer, Ph.D. The task is to characterize those electrode materials with UPS and KPFM so that information about the electronic structure of the electrode materials used in F. Ligmajers experiment is examined. This should support his experiment explanations and provide a building block for following studies of these materials and devices based on them.

The first chapter of this thesis provides basic information about electrochemistry and 1D nanostructures so the reader can better understand the motivation. The second chapter is dedicated to the electronic band structure of materials and to methods their measurement. In this part, the principle of the formation of energy bands in the solid is presented. It is also discussed how the band structure of different materials looks like and how it is related to some of the material properties. Last, the main methods of studying the band gap, the work function and the valence band edge position are presented. The third chapter is devoted to the principles of the experimental methods used in this work. Moreover, an additional chapter dedicated to the applications of KPFM is presented to provide a deeper insight on how this technique may be utilized for the study of different material properties. A special emphasis is put on the applications related to nanowires, nanotubes and electrochemistry. Even though some of the techniques are not directly related to the experimental part of the thesis, they are mentioned in the thesis to provide some general overview of other possibilities how nanowires can be analyzed for electrochemistry. In the experimental part, the strongest emphasis is put on the analysis

of the work function and the valence band edge position of WS_2 NTs and ITO. The aspects of spectra interpretation and possible obstacles of the UPS measurements are discussed. Since the UPS is surface sensitive, different sample preparation techniques are analyzed with the aim to obtain relevant data and to be able to avoid possible misinterpretation of the results.

1. Motivation - Electrochemistry

Electrochemistry is a usefull tool in many applications since it does not require expensive and complicated instrumentation. Some of the applications can be for example chemical and biological sensing (e.g. glucose sensors, gas detectors, pH meters), technological applications (e.g. electroplating), or energy storage (e.g. solar cells, batteries) [3]. An improvement in the particular applications might be achieved if novel materials are used, for example 1D nanostructures. This chapter provides a brief introduction to the field of electrochemistry as well as some general information about nanowires and nanotubes.

1.1. Introduction to electrochemistry

Electrochemistry is a branch of chemistry where charge carriers are utilized to study processes and reactions at the border between an electrode and an electrolyte. The object of study is an electrochemical cell – a system where the electrolyte is in contact with the electrodes. The electrolyte can then be studied via the electrodes by measuring the physical quantities such as current, potential, conductivity, charge or capacitance [4]. Electrochemical cells can be divided into two main types. If the electrochemical cell works as a voltage source because of spontaneous processes occurring on the electrodes, the cell is called a galvanic cell. If the electrolytic processes occurring on the electrodes are driven by external bias, the cell is called an electrolytic cell.

Any reaction happening at the electrode-electrolyte interface involves charge exchange, i.e. the oxidation states of atoms are changed. Both reduction processes (electrons are gained, oxidation state is decreased) and oxidation processes (electrons are removed, oxidation state is reduced) are always involved. Such redox (reduction-oxidation) reactions often occur between chemical species of the same phase, but the electrons can also be transferred through an interface (e.g. between a metal electrode and a molecule in aqueous solution). This kind of reaction can be written for example as [3]

$$\mathrm{O(aq)} + n\mathrm{e^-(m)} \underset{k_{\mathrm{ox}}}{\overset{k_{\mathrm{red}}}{\rightleftharpoons}} \mathrm{R^{n-}(aq)}, \tag{1.1}$$

where O and R are the oxidized and reduced forms of the redox couple in solution (aq), respectively. A number of n electrons are then transferred from the atom/molecule in oxidized state to the metal electrode and k_{red} and k_{ox} quantify the rate of reactions in the respective direction.

When the electrons are transferred from the electrolyte to the electrode or vice versa, the potential on the electrode changes. We are then interested in the potential difference between the electrode and the solution $\Delta\phi$. The relation of the potential difference and the concentrations of oxidized or reduced forms of the redox molecules in the solution (c_{O} and c_{R}, respectively) are described by Nernst equation [3]

$$\Delta\phi = \phi_0 - \frac{RT}{nF}\ln\frac{c_{\mathrm{O}}}{c_{\mathrm{R}}}, \tag{1.2}$$

where ϕ_0 is the standard electrode potential, R is the molar gas constant, F is the Faraday constant and T is the absolute temperature. A physical quantity that we can easily measure or control is a potential difference between two electrodes (i.e. the voltage)

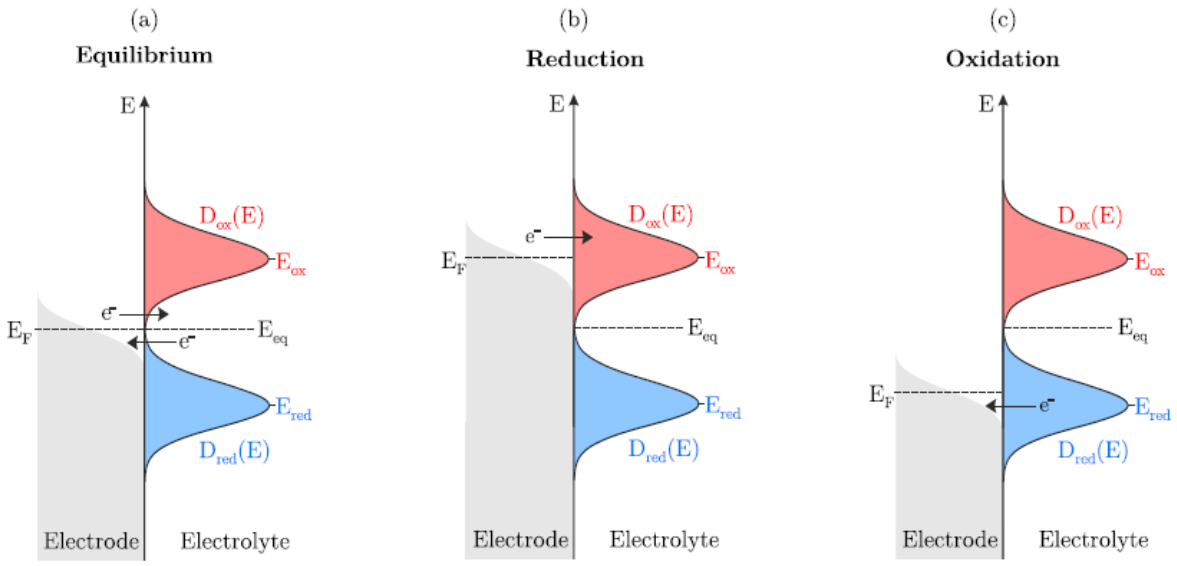

Fig. 1.1: *Electronic states at the interface between a metal electrode and a redox couple in (a) equilibrium, (b) with a negative potential applied (cathodic conditions), (c) with a positive potential applied (anodic conditions). Adopted from [3].*

and the Nernst equation reveals a relationship of the voltage between the electrodes and the concentrations of the oxidized or reduced forms of the molecules.

To better visualize the electron transfer between the electrode and the electrolyte, energy diagrams can be used (fig. 1.1) [3]. The electrode is described with a conduction band with states filled up to the Fermi level. The energy levels of the redox couple are described by the density of the oxidized states (empty) centered at energy E_{ox} and the density of the reduced states (filled) centered at the energy E_{red}. The energy levels of the oxidized and reduced states are located near the equilibrium Fermi level of the solution E_{eq} and split and broadened due to the interactions with the molecules of the solvent [3]. When a potential is applied on the electrode, electron transfer between the molecules and the electrode takes place, and the molecules are oxidized or reduced depending on the sign of the applied potential.

To make a conclusion from this brief introduction to the electrochemistry, it is important to know the position of the Fermi level and the energy levels of available states of the electrode material, especially when novel electrode materials are used. For example, such electrodes can be covered with nanowires or nanotubes, that promise better properties than conventional electrodes especially due to their high surface to volume ratio. And the purpose of the experimental part of this thesis is to evaluate this characteristics of the electrode materials.

1.2. Nanowires and nanotubes

Nanowires (NWs), nanotubes (NTs) and 1D nanostructures in general have been studied very extensively recently. This field seems to be very promising because 1D nanostructures offer high surface to volume ratio, which can be utilized for example in sensorics [5, 6] or photovoltaics [7]. Also 1D nanostructures often exhibit different electronic and structural properties compared to their bulk counterparts. For example, the stress

in the nanowire can be considerably lower compared to similar structure created by conventional lithographic methods, which can lead to reduced amount of defects. This stress is induced at the boundary between two materials due to the different lattice parameter (lattice mismatch). The nanowire growth is restricted only in one dimension so the stress in the nanowire lattice can be relaxed more easily. Therefore, nanowires or nanotubes can find an application also as field effect transistors (FET) [8] or photodetectors [9], for example.

The use of nanowires and nanotubes in electrochemistry is especially promising due to their high surface to volume ratio which allows electrochemical sensing with higher sensitivity (e.g. in [1]). The nanotubes can be useful for example due to their strong electrocatalytic activity and minimum surface fouling, in particular carbon nanotubes, which have been already quite extensively studied [10]. Inorganic nanotubes have not been studied so much and could provide interesting properties for improved applications. One of the examples can be WS_2-WSe_2 nanotubesu used in hydrogen evolution reaction [2].

Nanowires

Nanowires (NWs) are basically small wires with diameters in the range from ten to several hundreds nanometers and with the length of several microns or longer. Nowadays, nanowires can be grown either as homogenous wires (from single material) or as both axial and radial (core-shell) heterostructures [11]. Nanowires from various materials can be grown – metals (Al, Cu, Ti, W...) group IV semiconductors (Si, Ge...), III/V semiconductors (GaN, GaAs, InAs...), II/VI semiconductors (ZnS, CdS, ZnSe...), metal-oxides (ZnO, TiO_2, Al_2O_3...) or even perovskite or metal-organic nanowires [11, 12, 13, 14].

Nanotubes

Nanotubes (NTs) are also 1D materials with similar size as nanowires (i.e. 10–200 nm in diameter and hundreds of nm up to milimeters long). Nanotubes have been a subject of intensive study since the identification and description of carbon nanotubes in 1991 by Iijima [15], however, a trace to the first observation of nanotubes goes even back to 1952 [16]. Nanotubes are cyllindrical structures that can be imagined as if a 2D layer is rolled into a form of a tube. Nanotubes exist as both single-walled and multi-walled. Nowadays, apart from carbon, nanotubes from other different materials have already been prepared, such as WS_2, MoS_2, CeI_3, SnS-SnS_2 or even metal oxides such as VO_x and other [17].

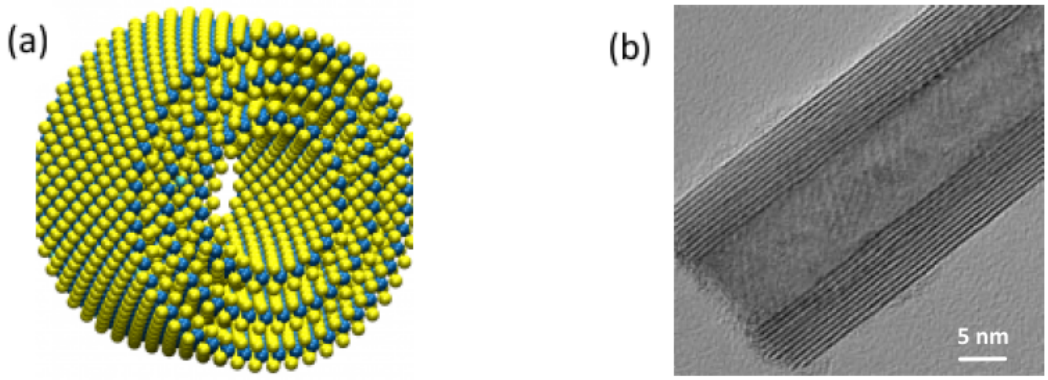

Fig. 1.2: *(a) Model of the structure of the WS_2 nanotube. Yellow atoms depict the sulfur and blue the tungsten. (b) TEM image of such nanotube where the layer structure is visible. Adapted from [18].*

2. Theoretical considerations

2.1. Band structure

This chapter is devoted to the basic introduction of the theoretical concept of electronic structure of materials, since it is very important for understanding their physical properties. A simple explanation of a band structure will be presented. For deeper explanations and further reading, a book by Ch. Kittel is recommended [19].

It was already in 1897 when sir J.J Thomson explored the existence of electron as a subatomic particle, being awarded a Nobel prize in 1906 [20]. He suggested the so called "plum pudding model" of the atom, where the atom consists of mixture of positive and negative particles. However, this model was soon improved by E. Rutherford, published in 1911 [21] after series of experiments, starting in 1908. In his group, H. Geiger and E. Mardsen shot alpha particles through Au foil. They detected some particles scattered under a degree higher than 90°, which Thomson's model could not explain. Rutherford then presented his model of the atom where the positive charge and mass are concentrated in a tiny nucleus of the atom. The next important step was N. Bohr's model of the atom, proposing that the electrons orbit around the nucleus on certain discrete levels. The electrons can perform a transition between those levels only if they receive specific amount of energy given as the energy difference between these levels [22]. It was later corrected by quantum mechanics to the point that we understand atoms now – the electrons are not localized and are not orbiting around the nucleus as Bohr proposed but are distributed with certain probability in atomic orbitals. However, his important remark that electrons in atoms can have only discrete values of energy is crucial for the explanation of many effects, including the formation of a band structure.

2.1.1. Electrons in atoms and the origin of band structure

According to the present understanding, atoms are formed of a tiny and heavy nucleus consisting of protons and neutrons, and electrons are arranged around the nucleus in orbitals, where each orbital has a specific discrete energy. This originates from the quantum mechanics – if electrons are trapped in a potential well, only certain electron wavefunctions are allowed, therefore they can exist only in certain states with discrete energies.

The states are described with 4 quantum numbers [23]. The principal quantum number n describes the atomic shell, giving us basic information about the energy and distance from the core (Fig. 2.1a). In spectroscopy, the atomic shells are often described by letters $K, L, M, N...$, having the same meaning as the principal quantum number $n = 1, 2, 3, 4....$ Next, we have the orbital quantum number l, which is related to the magnitude of an electron's angular momentum and describes the type of an orbital ($s, p, d, f... \sim l = 0, 1, 2, 3...$). Each orbital has slightly different energy (Fig. 2.1b, 2.1c) and possible values of l are $0, 1, ..., (n-1)$. Third quantum number we use for the description is magnetic quantum number m_l which is related to the orientation of the angular momentum vector in space. If the atom experiences magnetic field, the energy of orbitals split, depending on the magnetic quantum number. For each value of l, there are $2l + 1$ different values that m_l can have, so $m_l = \pm 1, \pm 2, ..., \pm l$. The last quantum number is the spin number m_s, referring to the intrinsic angular momentum of an electron. The m_s can have values of $\pm 1/2$, often referred to as "spin up" and "spin down".

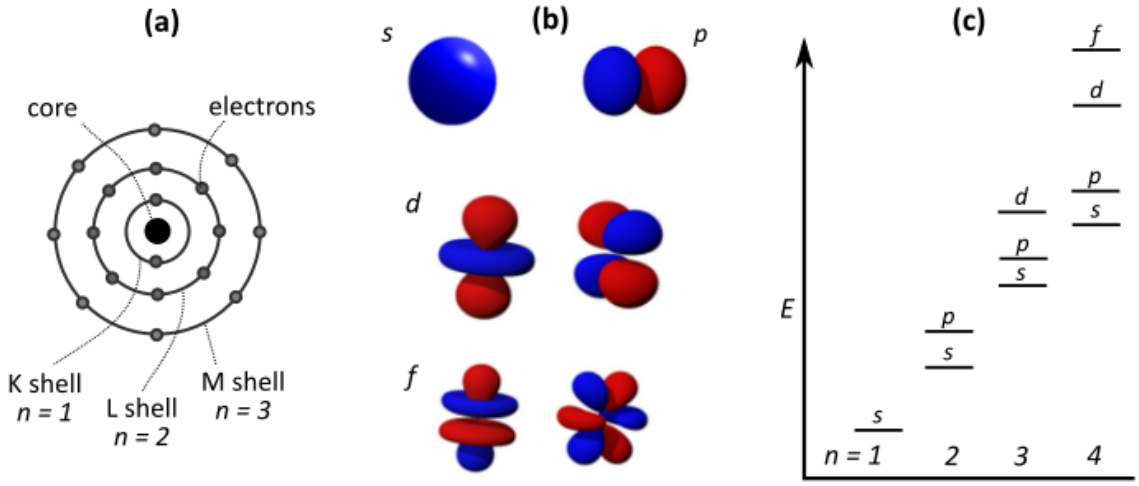

Fig. 2.1: *(a) Schematic drawing of atomic shells, where each shell represents one principal quantum number n. Each shell consists of one or more orbitals, represented by quantum number l. As n increases, the distance from the core and also the energy of the orbitals increases. (b) An example of possible shapes of the orbitals. (Note: p, d and f orbitals have total of 3, 5 and 7 possible shapes and space orientations with the same energy, respectively.) (c) Schematic diagram of the energy of orbitals with different principal quantum number. Adopted from [23] (a, c) and [24] (b) and edited.*

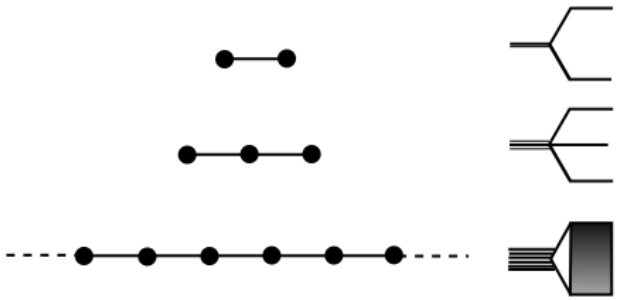

Fig. 2.2: *Schematic drawing of a formation of energy bands from the overlap of two, three, etc atomic orbitals. The overlap of many orbitals eventually results in formation of a band with a continuum of states. Adopted from [25] and edited.*

The state of an electron then can be fully described by this set of 4 quantum numbers. In Photoelectron Spectroscopy, usually the notation of an electronic state is for example $3p^{1/2}$, where $n = 3$, $l = 2$ (p-orbital) and the exponent denotes $j = l + s = 1 - 1/2 = 1/2$.

Now imagine we have two atoms of the same kind we want to bring close to each other. If the atoms are far away from each other, the energy of orbitals can be the same in both atoms. But as soon as the atoms are brought closer, electron wavefunctions start to overlap and the energy levels of orbitals split into two [25], because two electrons (one from the first atom and one from the second atom) cannot be in the same state due to the Pauli exclusion principle. If we bring more atoms together, the energy level of orbitals split into more levels and in the case of a crystal, the splitting results in the formation of energy bands [25] (many discrete states close together forming a so-called "quasi continuum"). The formation of bands is schematically described in Fig. 2.2.

This method of constructing the energy bands is called tight-binding approximation or more generally Linear Combination of Atomic Orbitals (LCAO) and more detailed description with proper mathematic formulation can be found for example in [25, chap. 3.8]. Another method for constructing the band structure is based on describing the valence electrons as "nearly free electrons" in periodic potential of the lattice with the use of Bloch functions, and its description can be found for example in [19, chap. 7]. Whereas the tight-binding approximation works well for deeper energy levels, the nearly free electron model works better for valence band electrons [26]. Another method for calculating the band structure is Density Functional Theory (DFT). The advantage of DFT is that it allows reducing the 3N dimensional problem (N is the number of atoms) of many-body Schrödinger equation to three dimensional problem of finding a minimum of the energy functional, which is equivalent to the quantum ground state [25].

2.1.2. Band structure of different materials

To describe how the electrons fill in the bands, it is necessary to introduce the density of states and the Fermi level. The density of states $\mathcal{D}(E)$ describes the number of states in a given interval of energies dE. For example, taking the simple case of 3D free electron gas (Fermi electron gas) bound in a box with finite size, it is possible to obtain the density of states by solving the Shrödinger equation for a free particle [19, chap. 6]. The density of states is then proportional to square root of energy $\mathcal{D}(E) \sim \sqrt{E}$. Then, if we have a certain amount of electrons, at 0 K, the electrons fill the states one by one from the state with the lowest possible energy up to the highest occupied state. The energy of this highest occupied state at 0 K temperature is called Fermi energy (Fermi level). This means that all states below Fermi level are occupied and all states above Fermi level are empty (Fig. 2.3). The integral of the density of states from zero to the Fermi level then gives us the total number of electrons $N_{el} = \int_0^{E_\mathrm{F}} \mathcal{D}(E)dE$.

The situation at elevated temperature is a little different, because some of the electrons can be excited to higher states by the thermal energy equal to $k_\mathrm{B}T$, where k_B is the Boltzman constant and T is temperature. Because electrons are fermions, their behavior is described by Fermi-Dirac statistics and the density of occupied states is modulated with Fermi-Dirac distribution function

$$f_\mathrm{FD}(E) = \frac{1}{e^{\frac{E-\mu}{k_\mathrm{B}T}} + 1}, \tag{2.1}$$

where E is the energy of the state and μ is chemical potential. At $T = 0$ K, the chemical potential is equal to the Fermi energy. The density of states of real crystals is, however, more complicated, because it is a combination of more bands with different density of states (Fig. 2.3)

As the combination of atomic orbitals from many atoms gives us the formation of energy bands, there are also regions outside the bands with forbidden energy (there are no possible states for electrons). Depending on how the band structure looks like, we can distinguish between insulators, metals, semi-metals and semiconductors (Fig. 2.4).

Each band has total of $2N$ states, where N is the number of primitive cells in the crystal and 2 accounts for the two possible spin orientations [19, chap. 7]. If we take for example diamond, it has an even number of electrons in its valence band, thus the whole band is

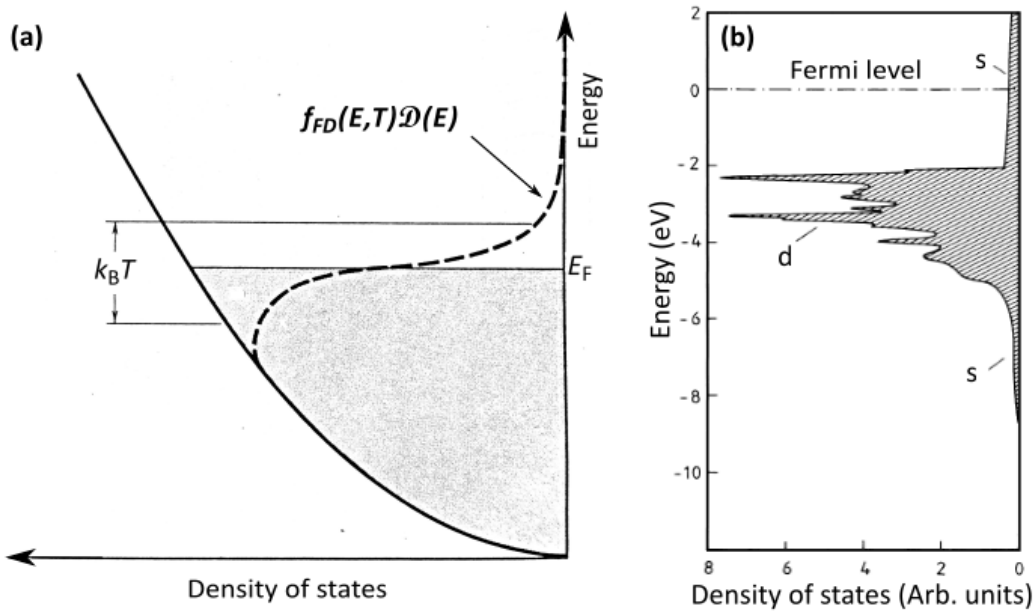

Fig. 2.3: *(a) Density of states of 3D free electron (Fermi) gas. At $T = 0$ K, all states are filled up to the Fermi level. At elevated temperature, some of the electrons are excited to higher state and the density of states is modulated by Fermi-Dirac distribution function. Adopted from [19] and edited. (b) Density of valence states of a real material (copper). Copper is a metal, so there are states available at the Fermi level position. Adopted from [27] and edited.*

filled and the Fermi energy lies somewhere in the gap of forbidden energies hence diamond is an insulator.

The first band below the Fermi level is called valence band and the first band above is the conduction band. The space between valence and conduction band where no states are available is called band gap.

Germanium, for example, has also an even number of valence electrons, so the valence band is also fully filled and the conduction band is empty. However, compared to the case of diamond, Germanium has a narrower band gap and at non-zero temperature, there is a certain probability (given by Fermi-Dirac statistics) that some of the electrons can be thermally excited to the conduction band.

With metals, the situation is different. Alkali metals have only one valence electron so the highest band is only half-filled. Another situation occurs for rare earth metals. Although they have two valence electrons and should form insulator or semiconductor, the bands are formed in such way that the two bands overlap and are both partially filled and form semi-metals. Because the Fermi level lies in the middle of a band, it makes no sense to distinguish between valence and conduction band.

In the case of doped semiconductors, additional electrons from the dopant atoms are introduced into the conduction band (n-type) or electrons from valence band are withdrawn from the band by the acceptor dopant atoms creating empty states in the valence band (p-type).

The reason why metals are conductive and insulators are non-conductive is that the states in the band are not only described by their energy, but also by a wave vector, which is related to the momentum [19, chap. 7]. If an external field is applied

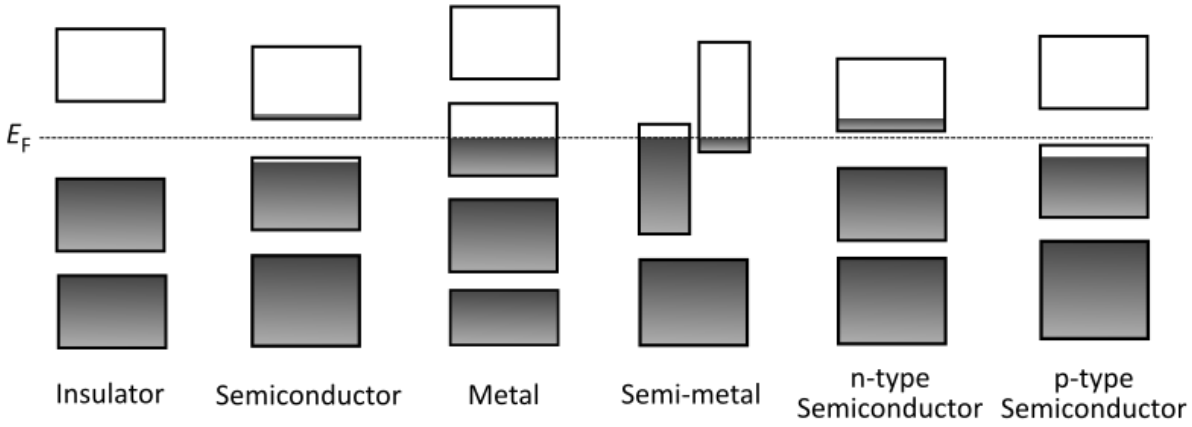

Fig. 2.4: *Schematic drawing of energy bands of different materials. For the case of insulators and semiconductors, the bands are fully filled and the Fermi level E_F lies in the band gap. Semiconductors have smaller band gap, so few of the electrons can be thermally excited from the valence band to the conduction band. For the case of metals and semimetals, the Fermi level lies inside a band. Doped semiconductors have the Fermi level shifted closer to the conduction (n-type) or valence (p-type) band because of additional donor (n-type) or acceptor (p-type) states. Adopted from [19] and edited.*

to an insulator (with magnitude small enough that does not destroy its electronic structure), continuous change in the momentum of electron is not possible because all other states in the band are occupied and the material is non-conductive. For the case of metals, the band is only partially filled and continuous change in momentum is possible, so the current can flow in the material [19, chap. 7].

The schematic band structure visualisation, as presented in Fig. 2.4, is often used to describe the electron structure of a material. Such a band structure is often described by several quantities, as shown in Fig. 2.5. The positions of the bands are usually referenced to the Fermi level E_F, or to the vacuum level E_{vac} (the energy of free electron in vacuum). The position of the Fermi level is given by a work function ϕ. In case of semiconductors and insulators more quantities are needed. E_g is the band gap, which is actually the energy difference between the top of the valence band E_v and the bottom of the conduction band E_c. The top of the valence band and the bottom of the conduction band can be also labeled HOMO (highest occupied molecular orbital) and LUMO (lowest unoccupied molecular orbital), respectively. The energy difference between the E_{vac} and E_v is an ionization potential IP (it is the energy needed to withdraw an electron and ionize the atom) and the difference between E_{vac} and E_c is an electron affinity χ (the energy released when an electron is added to an atom). Also, energy levels (states) E_{in-gap} inside the band gap can exist. Such state can belong for example to the level of dopants in intentionally doped semiconductor, to the surface states or to the states caused by impurities or defects in the material.

It is important to realize that the band diagram in a form of a "bar" bands described in previous paragraph is just a simplification of the electronic band structure. The energy of the electrons also depend on the momentum and the number of available states for given energy value inside a band is not constant and is described by the density of states, as shown in Fig. 2.3. However, such simplificated description is usually suffi-

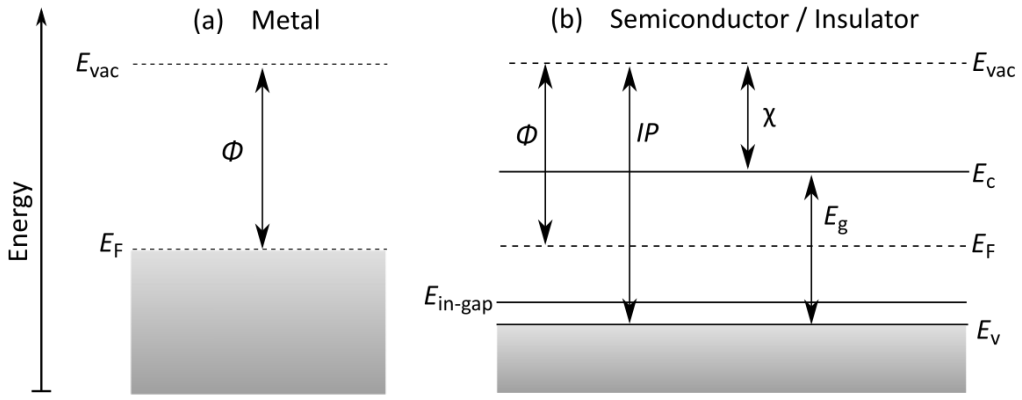

Fig. 2.5: *Schematic band structure of a metal and a semiconductor/insulator (the shaded area depicts filled states). The metal is characterized only by a work function ϕ. The Fermi level lies in the middle of a band. The semiconductor can be characterized with work function, ionization potential IP, electron affinity χ and band gap E_g. The Fermi level lies in the middle of the band gap. Also in-gap states can exist due to doping, defects or surface states.*

cient to describe some of the physical properties such as optical absorption and emission in the UV/visible spectrum, electrochemical activity or effects happening at the interface of two materials.

2.2. Methods of measuring a work function, band gap and Fermi level position

The band structure characteristic values described in the section above can not be measured with a single experimental technique. In order to describe the band structure, three characteristics always have to be known, for example the work function, the band gap and the position of the Fermi level in the gap (the "distance" from the valence band, for example). This section will provide an overview of the most common methods that can be used to investigate the work function, band gap and Fermi level position.

2.2.1. Measurement of a band gap

Probably the most common and the simplest method to determine the band gap is UV-Visible spectrometry. The sample is irradiated with variable wavelength monochromatic light, and the absorption coefficient α is measured (the absorption rate per unit length). The sample does not absorb almost any light when the energy of the light hf is lower than the band gap. If the energy of the light matches the band gap, the material starts to absorb, and we observe an absorption edge in the spectrum. The position of the absorption edge gives us an idea about the band gap. Additionally, more sophisticated methods can be used to evaluate the spectrum, such as "Tauc plot"[28]. In crystalline semiconductors, the following equation can be used to describe the relation between the absorption coefficient and the energy of light [29].

$$\alpha(f)hf \sim (hf - E_g)^m \,, \tag{2.2}$$

where m is an index that can have values of 1/2, 3/2, 2 and 3, which is related to the type of the absorption process such as direct or indirect transition and whether the transition is allowed or forbidden [29]. Then, the $\alpha(f)hf$ can be plotted versus $(hf - E_g)^m$, fitted with linear function and the intersection with $\alpha(f)hf$ axis then determines the band gap.

Another group of methods used to determine the band gap is based on temperature dependent electrical measurements. It is for example possible to extract the band gap from temperature dependent measurements of Hall coefficient [30]. It should be also possible to obtain information about the band gap from temperature dependent conductivity measurements. If the conductivity is measured in appropriate temperature range, it depends mainly on the intrinsic carrier concentration, which is proportional to $e^{-E_g/k_B T}$ [29].

2.2.2. Measurement of a work function

The work function measurement methods can be divided into two groups. One is based on the electron emission and the other on measuring the contact potential difference.

For example, Ultraviolet Photoelectron Spectroscopy (UPS) can be used to determine the work function. UPS is based on the photoelectric effect – when a sample is illuminated with UV light, electrons are emitted and the kinetic energy of the electrons is measured. This method is used in the experimental part of this thesis, so a special chapter is devoted to the Photoelectron Spectroscopy (chapter 3.1). Another method based on the photoelectric effect is Fowler method, which is based on measuring the amount of emitted electrons with respect to the illumination energy [31].

A Kelvin Probe method belongs to the latter group. This method utilizes two vibrating metal plate electrodes that work as a capacitor and the work function difference between them is measured. If the plates are vibrating, a voltage is induced in the circuit. However, if an additional external bias is applied between the capacitor plates, the voltage induced by the vibrations can be minimized to zero. This applied bias is then equal to the contact potential difference, which is given by the work function difference between the electrodes as $V_{CPD} = (\phi_{tip} - \phi_{sample})/-e$. A technique based on the same principle with much increased lateral resolution exists – the Kelvin Probe Force Microscopy (KPFM), which is also described in more detail in section 3.2.2.

2.2.3. Measurement of a valence and conduction band edge

The position of the valence band edge E_v and conduction band edge E_c can be determined also with photoelectron spectroscopy (see section 3.1.3). With UPS, however, it is possible to analyze only states filled with electrons, i.e. the valence band. To analyze the empty states, Inverse Photoelectron Electron Spectroscopy can be used. As the name suggests, this method is virtually the opposite to the Photoelectron Spectroscopy – electrons with given energy impinge on the sample and emit light when they are decelerated [32]. This can be viewed as a process where incoming electron in an initial state is decelerated to the final state and emits light equal to the energy difference between them. Then the intensity of emitted light at fixed wavelength is recorded while varying the impinging electron energy or the energy of the electron can be constant and wavelength-intensity dependence is recorded.

Another method how to analyze both filled and empty states is Scanning Tunnelling Spectroscopy (STS). This method uses a sharp tip that is brought close to the surface of a sample and a tunnelling current between the tip and sample is measured, if a bias is applied on the tip. If the bias is swept across various voltages, a spectrum is recorded, giving information about the local density of states in the sample. The advantage of STS is ultimate lateral resolution in nanometers, but the biggest disadvantage is that it only measures the states localized exactly at the surface, extending to the vacuum, because they need to interfere with the tip. States localized even one or two atomic layers deeper are not measured [33]. Another method how to analyze both filled and empty states is Scanning Tunnelling Spectroscopy (STS). This method uses a sharp tip that is brought close to the surface of a sample and a tunnelling current between the tip and sample is measured, if bias is applied on the tip. If the bias is swept across various voltages, a spectrum is recorded, giving information about the local density of states in the sample. The advantage of STS is ultimate lateral resolution in nanometers, but the biggest disadvantage is that it only measures the states localized exactly at the surface, extending to the vacuum, because they need to interfere with the tip. States localized even one or two atomic layers deeper are not measured [33].

3. Experimental methods

3.1. PES - Photoelectron Spectroscopy

Photoelectron Spectroscopy is a general term for experimental techniques used to study the surface of a material. The principle of this method is based on photoelectric effect, which was first observed by H. Hertz in 1887 and later described in more detail by A. Einstein in 1921 [34]. If a metal is illuminated by light with energy given by $E = hf$, electrons are emitted from the material if the light's energy is sufficient. The kinetic energy of emitted electron depends on the energy of incident photon E and on a material property Φ called work function as $E = hf - \Phi$. The work function then describes minimum energy needed to withdraw an electron from the metal. Not only metals do exhibit the photoelectric effect, but all materials. However, the work function in semiconductors and insulators has slightly different meaning. In general, the work function describes the energy difference between Fermi level and vacuum level, as described in section 2.1.2. Semiconductors and insulators can be additionally described by another characteristics called ionization potential (IP), which is essentially the energy difference between the vacuum level and the energy of the highest occupied molecular orbital (HOMO).

Photoelectron Spectroscopy can be divided into two subgroups, depending on the light used for illumination – XPS (X-ray Photoelectron Spectroscopy) and UPS (Ultraviolet Photoelectron Spectroscopy) in which X-ray or UV light is used, respectively. In both techniques, a spectrum of emitted photoelectrons is recorded, displaying the number of electrons emitted per unit time depending on their kinetic energy. In XPS, the material is irradiated by X-rays, which have enough energy to excite core electron energy levels. XPS is mainly used for chemical analysis, giving us information about the chemical composition and also the chemical state of the particular element. UPS is used to study the valence electrons which are more weakly bound than core electrons, and thus excitation light of lower energy (UV) can be used. It can provide information about the density of states in valence band, band structure and some relevant parameters concerning the interaction between interfaces, such as work function or Fermi level position, which are important subjects of this work.

3.1.1. Basic principles

Electrons in atoms are arranged in orbitals around the nucleus as described in chapter 2. We can describe the electrons sitting on orbitals by "binding energy", which is in fact the amount of energy needed to extract electron from the orbital so it becomes a free electron. Using radiation with sufficient energy, we are able to ionize the atom in this way and we can measure the kinetic energy of the emitted electrons, which is given by:

$$E_{\mathrm{k}} = hf – E_{\mathrm{B}}, \tag{3.1}$$

where E_{B} is the binding energy of the orbital that the electron comes from and hf is the energy of irradiating photon.

Another process occurs right after this photoemission in order to relax the ion. Empty hole in the inner shell left by emitted photoelectron is rather filled by electron from higher level. The excess of energy can be either emitted in the form of a photon or balanced by

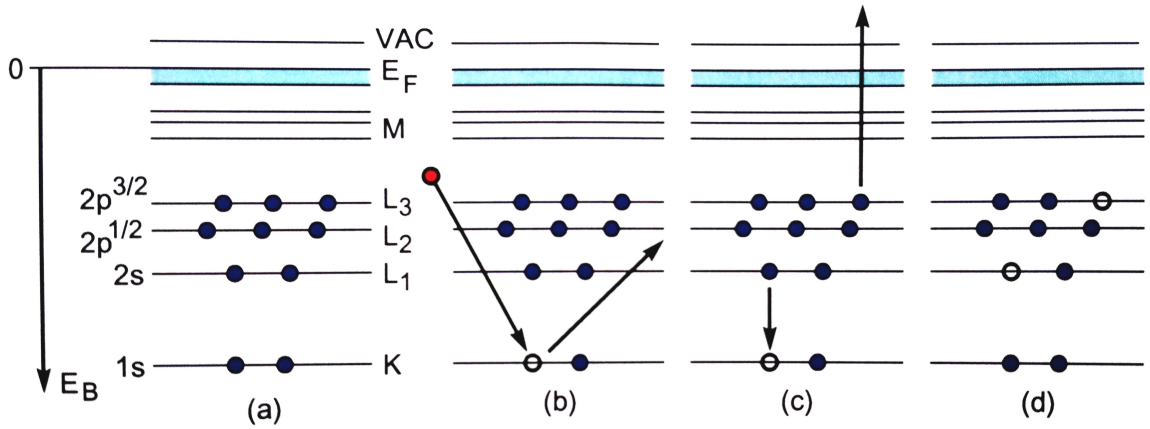

Fig. 3.1: *The principle of photoemission and Auger process. (a) The atom in its initial state. (b) The incident X-ray photon knocks off a core level electron allowing it to escape the material. The hole left behind the photoelectron is filled with an electron from higher levels. The excess of energy can be either radiated in a form of a photon, or (c) another electron called Auger electron is emitted. (d) The final state of the atom after the Auger electron emission. Adopted from [35].*

the emission of another electron called "Auger electron". The Auger electron can be also detected together with photoelectrons and its kinetic energy is

$$E_{\mathrm{k,ae}} = E_{\mathrm{B1}} - E_{\mathrm{B2}} - E_{\mathrm{B3}}, \tag{3.2}$$

where E_{B1} is the binding energy of the first emitted photoelectron, E_{B2} is the initial binding energy of the relaxing electron and E_{B3} is the binding energy of Auger electron. The notation of Auger transitions consists of the element and 3 letters (e.g. O KLL): The first letter describes the shell of the initial vacancy, the second the initial shell of the relaxing electron and the third the shell that the Auger electron is emitted from. Unlike the photoelectron, kinetic energy of which depends on the incident photon energy, the Auger electron kinetic energy depends only on the difference between energy levels, which is characteristic for each element. Both processes are schematically described in Fig. 3.1.

In practice, the binding energy is referred to the Fermi level instead of the vacuum level as described above. In order to achieve that, the spectrometer should be in conductive connection with the sample, and new term of the spectrometer work function ϕ_s should be subtracted from the right side of both equations 3.1 and 3.2.

When the sample is irradiated, all the electrons, from tight-bound core to less-bound valence electrons are affected by this photoelectric effect. As already indicated above, PES is a surface sensitive technique. Even though the X-rays are able to penetrate quite deep in the sample, the surface sensitivity is given by the ability of electrons to escape from the surface of the material, which is closely related to the inelastic electron mean free path λ. This parameter usually varies between 1 to 10 nm and is dependent on the kinetic energy of the electron and on the material the electron should cross before escaping the surface [37]. For illustration, the dependence of inelastic mean free path on kinetic energy is displayed in fig. 3.2.

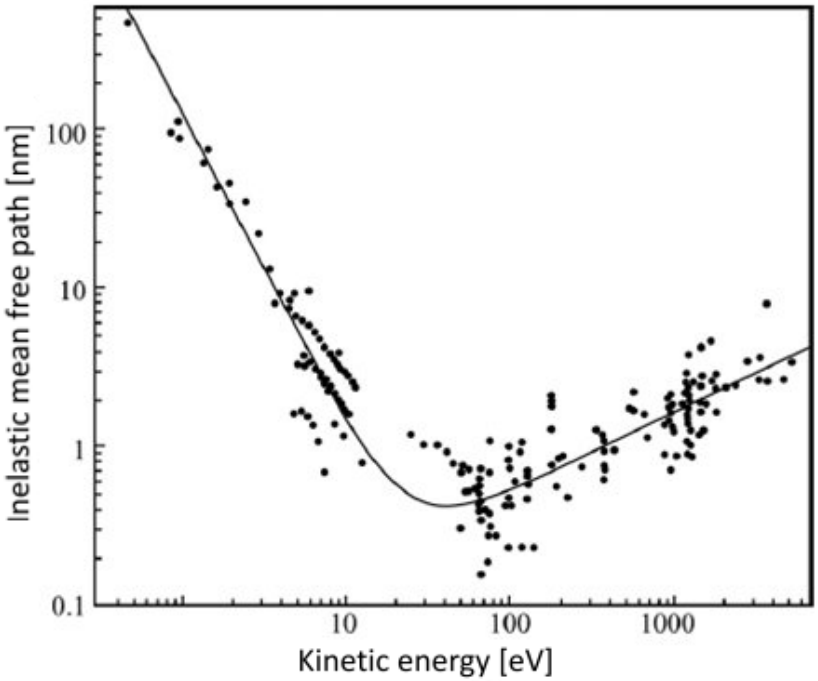

Fig. 3.2: *A compilation of measured inelastic mean free path of an electron versus its kinetic energy for different materials by Seah et. al. The solid line presents a theoretical curve fit. Adopted from [36] and edited.*

3.1.2. Instrumentation

In PES we want to avoid additional scattering of the emitted electrons, therefore UHV (Ultra High Vacuum) is needed. Basic apparatus scheme of a PES instrument is shown in fig. 3.3. The source of UV/X-ray light irradiates the sample, photoelectrons emitted from the sample are captured by the input electron optics and transmitted to the hemispherical analyzer which is set to the energy we want to detect. Only electrons with this given energy can pass through the analyzer and can be captured by the detector.

It is worth noting, that the instrument is usually constructed in such a way that the angle between the source and the analyzer is about 54.7°. The reason for this configuration is the existence of a so-called "magic angle". If the angle between the source and and the analyzer is equal to this "magic angle", the angular asymmetry parameter is a constant, and therefore it does not have to be included in the expressions for quantification [38].

X-Ray Source

Probably the most common X-ray sources in laboratory instruments are Mg and Al anodes, because Al K_α and Mg K_α spectral lines (with energies of 1486.6 eV and 1256.6 eV, respectively) have enough energy to knock-off the electron from the inner orbital levels of atoms and are narrow enough to be used also without monochromator. The scheme of such source is described in Fig. 3.4.

In order to achieve higher resolution, monochromatic source can be used. The monochromation can be achieved for example with a Rowland circle monochromator which is shown in Fig. 3.5.

Spectrometer

The spectrometer consists of the electron optics, the analyzer and the detector. Electrons that escaped from the sample are collected by the input electron optics. The main function of the electron optics is to slow down and focus the electrons to the spectrometer. The spectrometer consists of two concentric hemispherical electrodes, each on different potential. Because of the field between them, only electrons with certain energy (or close to this energy) depending on the potential applied to the hemispheres, can get through the analyzer to the detector, which counts the number of electrons transmitted through the analyzer.

The spectrometer is usually operated in "Constant analysis energy mode", which means that the spectrometer is set to one energy (called pass energy) only and the incoming electrons are slowed down to this particular energy by the electron optics. This allows to achieve constant resolution throughout the whole energy spectrum [37].

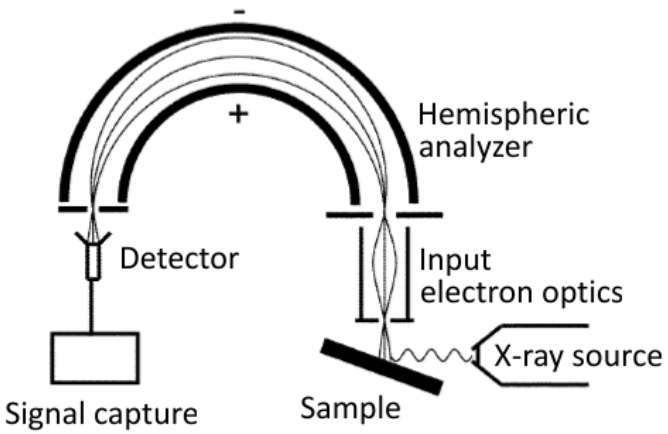

Fig. 3.3: *A scheme of an experimental setup. Electrons emitted from the sample are focused and slowed by the input electron optics to the hemispherical analyzer. Electrons only in narrow range of kinetic energies can pass through the analyzer. Adopted from [39].*

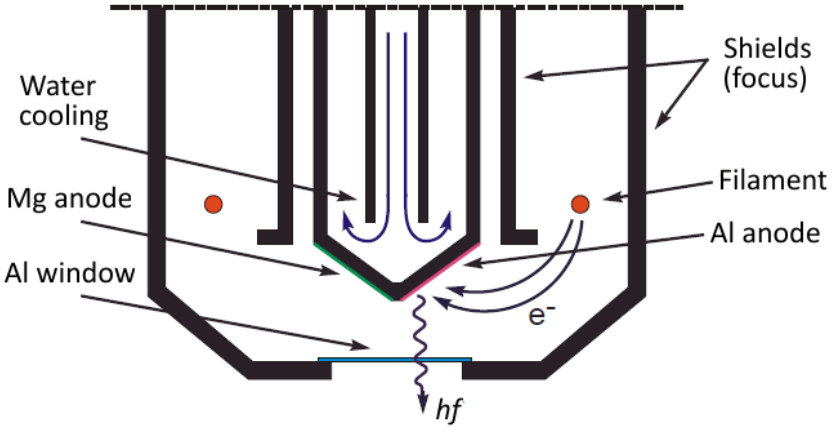

Fig. 3.4: *A scheme of a twin anode X-ray source with Mg (1253.6 eV) and Al (1486.6 eV) anode. Adopted from [40].*

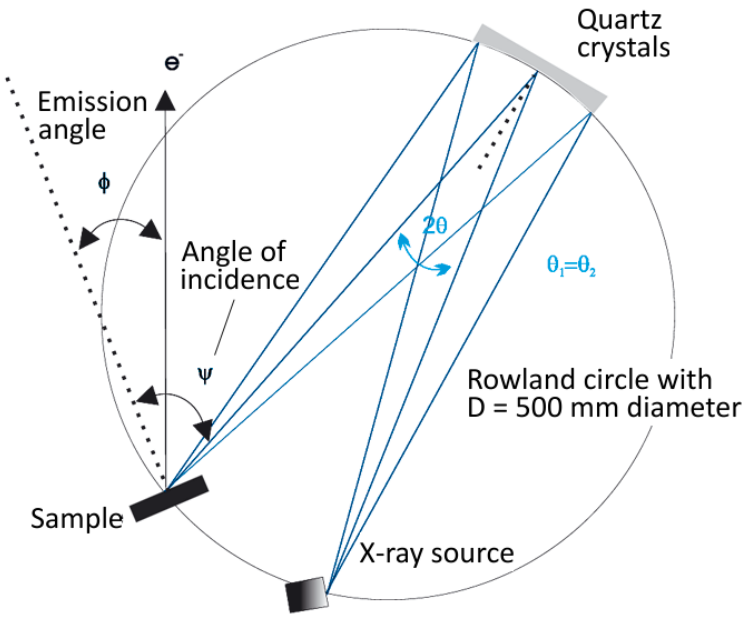

Fig. 3.5: *A scheme of Rowland monochromator. The monochromation of the X-rays is achieved via diffraction on quartz crystal. Adopted from [41].*

Detection and imaging

The detection and counting of photoelectrons can be achieved by a common MCP (Micro-Channel Plate) detector. However, modern PES instruments usually offer also an "imaging mode" allowing spatial resolved chemical analysis. This can be achieved by several approaches [42]. One of them utilizes the fact that the electrons passing through the hemispherical analyzer are also spatially dispersed around the circumference and can be detected for example by a delay-line detector [43]. Other ways how to achieve spatially resolved image can be scanning the field of view of the input electron lens system or scanning the X-ray beam itself (by scanning the electron beam across the anode) [42].

3.1.3. Spectra

By collecting the photoelectrons and counting them we get the spectrum which is displayed as a plot of the electron count versus the kinetic or binding energy, according to the equation 3.1. The sample is usually in a conductive connection with the spectrometer and the binding energy is referred to the Fermi level. Therefore, work function of the spectrometer has to be also accounted as described in section 3.1.1. As a result, Fermi level appears at zero binding energy.

XPS

The measured spectrum consists of main photoelectron lines, Auger peaks, characteristic background and additional features arising from various side processes. An example of XPS spectrum of Indium Tin Oxide (ITO) is shown in Fig. 3.6.

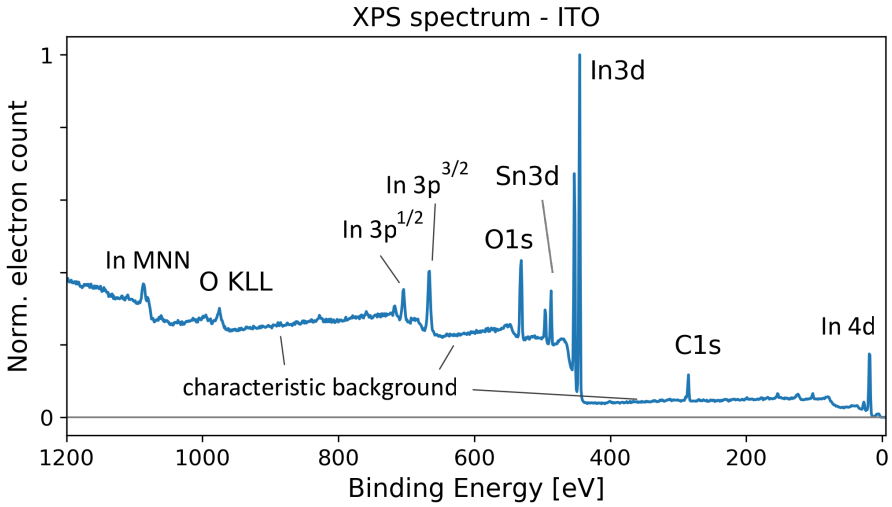

Fig. 3.6: *An example of XPS spectrum. Main photoelectron peaks from Indium Tin Oxide (ITO) are identified (In 3d, Sn 3d, O 1s) and C 1s photoelectron peak from adventitious carbon contamination. Also Auger electron peak O KLL is visible in this spectrum. Other unlabelled peaks refer to other photoelectron or Auger transitions arising from both ITO and surface contamination.*

To identify the chemical composition, the main features to look at are the photoelectron peaks (e.g. Au 4f or C 1s peak). The position of the peaks gives information about the element and the orbital it was ejected from, whereas the peak intensity can provide information about relative element concentration by comparing the peak area of each compound (a special care must be taken because the probability of each electron emission and detection can be different and depends on the element, on its kinetic energy, the depth it escapes from and the analyzer transmission). The photoelectron line can appear as two separate peaks due the spin orbit splitting (a dublet). In fact, only s orbitals have single line and other orbitals (p, d, f...) are affected by spin orbit splitting (e.g. In $3p^{1/2}$ and In $3p^{1/2}$). The intensity ratio of the dublet peaks depends only on the angular momentum l of the level, but the distance between them also depends on the atomic number Z [37]. The width of a photoelectron line is given by convolution of the natural line width (originating from Heisenberg's uncertainty principle), the shape of the source spectral line and the analyzer characteristics. These lines are usually symmetrical; however, for the case of metals, the shape can be asymmetric due to coupling with conduction electrons [43].

In the XPS spectrum, we can also observe characteristic background that rises for higher binding (lower kinetic) energies after each spectrum line. This signal increase is caused by electrons escaping from certain depth (not very far from surface), which had lost a random amount of energy due to inelastic scattering with atoms of the solid [37].

Auger electrons can also be observed in the spectrum. They can be used for example for identifying the elements, if main photoelectron peaks overlap.

There are also other features and additional peaks that can be observed in the spectrum [43, Chap. E]. For example, satellite peaks can be observed as a result of multiple line excitation source. More additional peaks can also appear in case some of the atoms end up in excited ionized state after the photoelectric effect, which causes the photoelectron kinetic energy to be lower. Other effects worth mentioning are for example multiplet splitting or plasmon losses.

The chemical state can be obtained from the exact position of the photoelectron peak [37, 43]. When the atom is bound to another atom, the energy levels of core electrons are slightly different, which can be observed as a shift of the photoelectron peak position. However, determining the absolute position of the peak is not straightforward due to possible charge accumulation on the sample, which causes a shift of the whole spectrum. In order to overcome this effect, internal calibration is usually done using photoelectron peak that appears almost always at the same energy. Adventitious carbon at binding energy of 284.8 eV is a common reference peak. This charge accumulation effect becomes significant especially when measuring poor conductors or insulators. In order to minimize this effect, neutralizer or flood gun, providing a flow of low energy electrons to the sample, can be used to compensate for the electron loss due to the photoelectric effect.

UPS

The principle of obtaining UPS spectrum is the same as for the XPS spectrum with the difference that we use UV source, which excites only valence levels. In addition, the advantage of UPS is that the standard UV source (He discharge lamp) has a narrower line shape and higher intensity compared to common X-ray sources [37]. The UPS spectrum, however, does not contain only peaks corresponding to valence band levels. In certain cases it is possible to determine the work function of the surface and the position of highest occupied molecular orbital (HOMO) with respect to Fermi level, as described in Fig. 2.4 in section 2.1.2. It is necessary to emphasize that UPS measurements are generally more complicated than XPS because the shape of the spectrum can be affected by several effects such as different charging, radiation damage, surface contaminants or sputtering effects, which are rather difficult to detect and avoid.

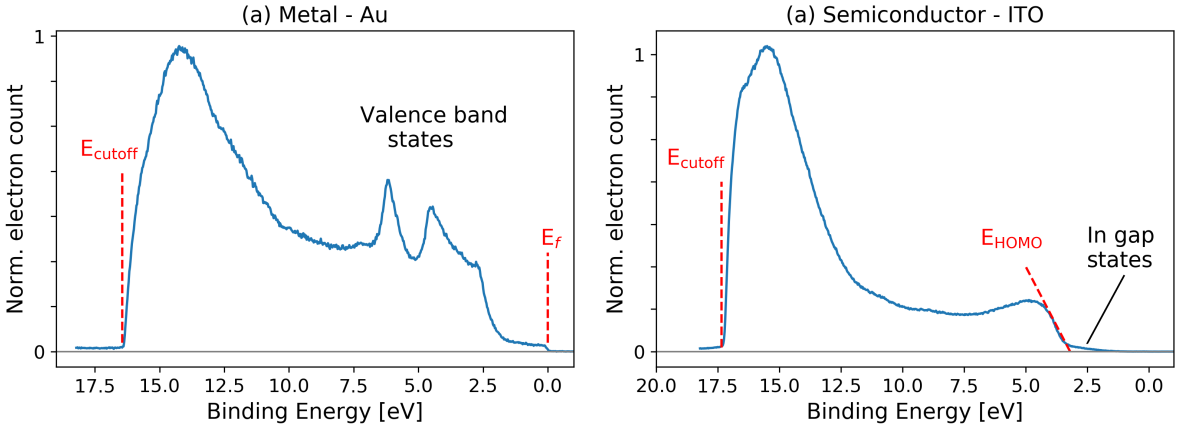

Fig. 3.7: *An example of a UPS spectrum of (a) a metal (Au) and (b) a semiconductor (ITO). The cutoff energy on the high binding energy side of the spectrum determines the work function of the material. For the case of metals, the signal should drop to zero at the Fermi level E_F (zero binding energy) and this can be used as a charge referrence. For the case of materials with a band gap, the Fermi level should lie also at zero binding energy, but is not visible in the spectrum (there are no electrons on the Fermi level). However, the energy of the highest occupied molecular orbital E_{HOMO} can be extracted and the presence of in-gap states is can be detected as well.*

The interpretation of UPS spectrum can be explained on the sample spectrum of Au and ITO shown in Fig. 3.7. The high binding energy edge of the spectrum allows us to determine the work function as follows:

$$\Phi = hf - E_{\text{cutoff}}. \tag{3.3}$$

The position of the high binding energy edge E_{cutoff} corresponds to the deepest bound detectable electrons. Those electrons have to overcome the work function Φ of the material. Therefore, the work function is given by the difference between excitation light energy and the energy at cutoff position.

For the case of metals, we can clearly observe the position of Fermi level at zero binding energy (i.e. electrons with maximum kinetic energy). For the case of semiconductors, the position of the low binding energy edge of the spectrum determines the position of HOMO energy with respect to the Fermi level. Then, we can also determine the ionization potential IP given by:

$$IP = hf - E_{\text{cutoff}} + E_{\text{HOMO}}. \tag{3.4}$$

However, special care must be taken at the position of the Fermi level in the spectrum because it is not directly determined, and hence it cannot be used as a reference. Therefore, in case the sample is not well conductive and charging might occur, it can result in the shift of the spectrum and wrong determination of both work function and HOMO energy.

3.2. SPM – Scanning Probe Microscopy

Great advances in the research of surfaces and micro- and nanostructures were made possible after the development of the Scanning Probe Microscopy. The principle of SPM is based on having a small probe, usually a very sharp tip, which can examine and measure the properties of the surface including not only topography, but also local electrical or magnetic characteristics.

The origins of SPM trace back to 1982, when G. Binning and H. Rohrer published the principle of Scanning Tunnelling Microscope (STM), which allowed the direct study of surfaces with atomic resolution. For this invention they received a Nobel Prize in 1986. The principle of STM is based on measuring the tunnelling current between the tip and the sample. However, serious limitation of STM is that it can be only used to study conductive samples [44]. In order to overcome this drawback, Atomic Force Microscopy (AFM) was developed [45], which allowed topography measurements of nonconductive samples as well. Later, many other techniques based on AFM were also developed, such as KPFM (Kelvin Probe Force Microscopy), C-AFM (Conductive AFM) or MFM (Magnetic Force Microscopy) [46, 47], allowing local examination of also other material properties.

Because many of the techniques used to study local properties of surfaces and nanostructures are derived from AFM, in the next part, basic principles of AFM will be described.

3.2.1. AFM – Atomic Force Microscopy

Atomic Fore Microscopy is used to study the topography of measured samples commonly with nanometer resolution, possibly even down to molecular and atomic resolution [48]. The crucial part of AFM is a sharp tip (usually with a tip radius of about 10 nm [47]) mounted on a flexible cantilever, whose exact position is recorded.

When the tip is brought close to a surface, a force interaction between the tip and the sample takes place. This interaction is approximately described by Lennard-Jones potential, which is an expression consisting of combination of attractive van der Waals interaction (larger tip-sample distances) and repulsive interaction caused by Pauli exclusion principle due to atomic orbitals overlapping (smaller tip-sample distances) [47]:

$$U(r) = 4\varepsilon \left[\left(\frac{\sigma_0}{r} \right)^{12} - \left(\frac{\sigma_0}{r} \right)^{6} \right], \tag{3.5}$$

where r is the inter-atomic distance, ε accounts for the depth of the potential well and σ_0 is the distance corresponding to zero potential value.

For the detection of the position of the tip, a laser-photodiode system is used, as shown in Fig. 3.8. The light beam from a laser diode is reflected from the cantilever and detected on a 4-segment photodiode. The position of the cantilever is detected by evaluating the magnitude of the signal in each quadrant. The difference between upper and lower quadrants determines the vertical position of the tip while the difference between left and right quadrants gives information about the torsional bending of the cantilever.

The AFM can operate in three different regimes – contact, semi-contact and non-contact regime. In the contact regime, the tip is pressed to the surface which causes bending of the cantilever, corresponding to a certain force. Then, the tip is scanned across the sample recording the topography, which can be performed in two modes, depending on the feedback system. In constant height mode, the distance between the tip and and the sample is kept constant and the difference in cantilever bending is recorded. In constant force mode, the cantilever bending is kept constant and the z-position of tip (or the sample) is adjusted in order to maintain constant force acting between the tip and sample. In non-contact regime, the tip is oscillated at or near its resonance frequency slightly above the sample, in the region where attractive van der Waals forces are dominant. If the tip-sample distance changes, the force changes, which leads to the change in the resonance frequency, and hence also to the change in the amplitude of the oscillations. Again, we distinguish two modes – Amplitude Modulation, where the feedback maintains the amplitude constant by adjusting the tip-sample distance and Frequency Modulation, where the driving amplitude is set constant and the change in resonance frequency is directly measured and the feedback system adjusts the tip-sample distance to maintain the frequency shift constant [44]. The last is the semi-contact regime, which is very similar to the non-contact regime, only the amplitude of the oscillations is higher and the tip enters also the repulsive region during the oscillation cycle. This mode is sometimes also called "Tapping mode".

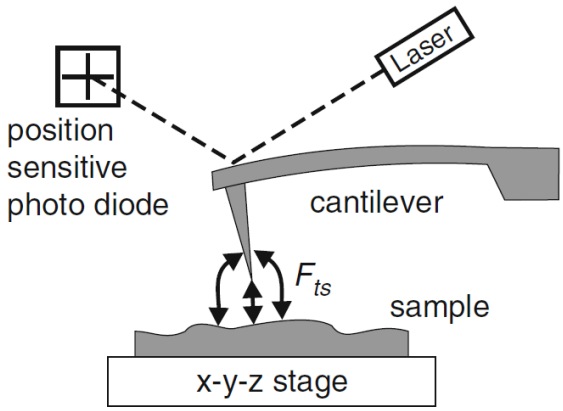

Fig. 3.8: *Working principle of an AFM. The position of the cantilever is detected using a laser beam and position sensitive photodiode. The scanning can be done either by the tip or the sample using the piezo-driven x-y-z stage (depending on the particular instrument). Adopted from [44].*

3.2.2. KPFM – Kelvin Probe Force Microscopy

Detailed description of KPFM can be found in book by S. Sadewasser and T. Glatzel [44]. In this section, the basics of KPFM are presented together with some other remarks from different resources.

The principle of KPFM is basically adopted from the principle of Kelvin probe invented by Lord Kelvin in 1898. The Kelvin Probe utilizes two parallel vibrating capacitor plates. If a specific voltage on one of the plates is applied, the current induced in the circuit is zero. It is, however, not convenient to use the same detection mechanism on microscopic scale – when the area of capacitor plates is reduced, the current induced is very small and the measurement is significantly limited by the sensitivity. For that reason, the KPFM utilizes the same physical principle, but analyses electrostatic forces acting on the tip instead of the current [44].

Kelvin Probe Force Microscopy is a combination of non-contact atomic force microscopy and Kelvin probe. The principle is described in Fig. 3.9. The tip is oscillated in a certain distance above the surface and when the tip is brought close to the surface, electrostatic forces start to act due to a difference in the Fermi levels of the tip and the sample. With a method described later, it is possible to obtain the contact potential difference (CPD), which is given by the difference between the work functions of the tip Φ_t and sample Φ_S as:

$$V_{\mathrm{CPD}} = \frac{\phi_{\mathrm{tip}} - \phi_{\mathrm{sample}}}{-e}, \tag{3.6}$$

where e is elementary charge. Hence, for obtaining the work function of the sample, the work function of tip must be known or a reference measurement on a sample with known work function must be carried out.

The KPFM measurement is performed in a two-pass mode – the sample is line-scanned, while each line is measured twice: In the first pass, the topography is measured by standard AFM, then in the second pass, the tip is lifted to a certain height above the surface and is moved in this constant height in order to minimize topography crosstalk to the KPFM measurement. During the second pass, if an AC voltage V_{AC} with a fre-

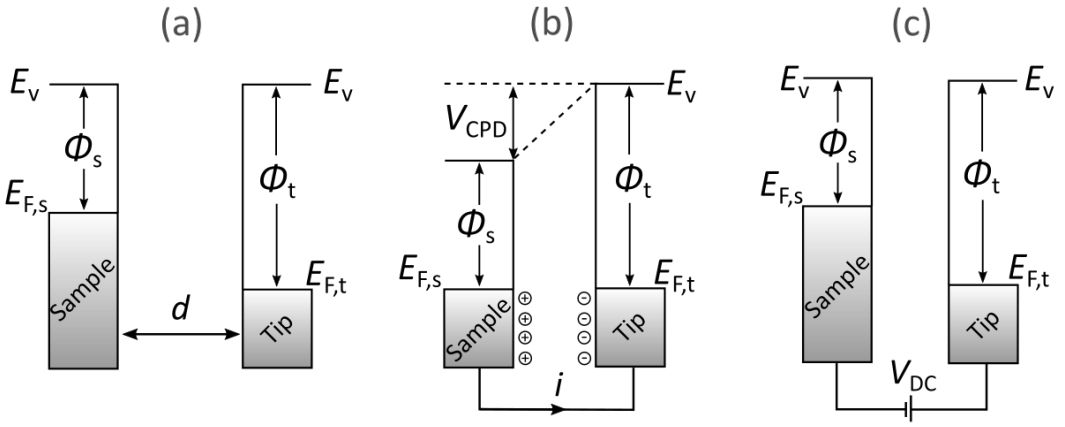

Fig. 3.9: *Schematic drawing of the work function and Fermi level position of the tip and the sample to illustrate the KPFM principle. (a) The tip is far away from the sample. (b) When the tip is brought closer to the sample and conductive connection is formed, a current i starts to flow between the tip and the sample until the Fermi levels are aligned. The difference between the vacuum level E_v of the tip and sample is the contact potential difference (V_{CPD}). Due to the V_{CPD}, an electrical force acts on the contact area. (c) This electrical force can be nullified when an external DC bias is applied between the tip and the sample and the magnitude of the bias is then equal to the V_{CPD}. Adopted from [49] and edited.*

quency ω and DC voltage V_{DC} is applied to the tip, the electrostatic force acting between the tip and the sample is given by [44]:

$$F(z,t) = -\frac{1}{2}\frac{\partial C(z)}{\partial z}\left[(V_{DC} \pm V_{CPD}) + V_{AC}\sin(\omega t)\right]^2, \tag{3.7}$$

where z is the coordinate perpendicular to the samples surface and $\partial C/\partial z$ is capacity gradient between tip and sample. This electrostatic interaction can be separated into three contributions [44]:

$$F_{DC} = \frac{\partial C(z)}{\partial z}\left[\frac{1}{2}(V_{DC} \pm V_{CPD})^2\right], \tag{3.8}$$

$$F_{\omega} = -\frac{\partial C(z)}{\partial z}(V_{DC} \pm V_{CPD})V_{AC}\sin(\omega t), \tag{3.9}$$

$$F_{2\omega} = \frac{\partial C(z)}{\partial z}\frac{1}{4}V_{AC}^2[cos(\omega t) - 1]. \tag{3.10}$$

F_{DC} is a constant term corresponding to static cantilever bending, F_{ω} is used for the evaluation of V_{CPD} and $F_{2\omega}$ is used in capacitive microscopy [49]. The $\pm$ sign denotes whether the voltage is applied to the tip $(-)$ or to the sample $(+)$. If we look at the F_{ω} term, we can see that it is possible to eliminate this contribution by applying voltage equal to the V_{CPD}.

The fact that the KPFM measurements are performed in two-pass mode brings also several disadvantages [44]. The piezoceramics, used for the precise positioning of the tip and sample, can exhibit a delay in a response for the abrupt change in applied voltage,

therefore the tip-sample distance can be in reality different than the expected distance given by the voltage applied to the piezo-element. This effect as well as the temperature drift could be responsible for inaccurate topography determination. In that case, the tip-sample distance is not constant which brings errors to the KPFM measurement. Moreover, sometimes it may be important to account for electrostatic interactions due to the CPD differences also in the first topography pass, where it can also induce another error [50]. The fact that the KPFM measurements are performed in two-pass mode brings also several disadvantages [44]. The piezoceramics, used for the precise positioning of the tip and sample, can exhibit a delay in a response for the abrupt change in applied voltage, therefore the tip-sample distance can be in reality different than the expected distance given by the voltage applied to the piezo-element. This effect as well as the temperature drift could be responsible for inaccurate topography determination. In that case, the tip-sample distance is not constant which brings errors to the KPFM measurement. Moreover, sometimes it may be important to account for electrostatic interactions due to the CPD differences also in the first topography pass, where it can also induce another error [50]. The fact that the KPFM measurements are performed in two-pass mode brings also several disadvantages [44]. The piezoceramics, used for the precise positioning of the tip and sample, can exhibit a delay in a response for the abrupt change in applied voltage, therefore the tip-sample distance can be in reality different than the expected distance given by the voltage applied to the piezo-element. This effect as well as the temperature drift could be responsible for inaccurate topography determination. In that case, the tip-sample distance is not constant which brings errors to the KPFM measurement. Moreover, sometimes it may be important to account for electrostatic interactions due to the CPD differences also in the first topography pass, where it can also induce another error [50].

There are also other things important to realize when performing KPFM measurements. For example the electrostatic interaction used for determination of CPD is not only dependent on the very small measured point, but also on the surroundings and the tip and cantilever shape. When the tip is lifted in the second pass, larger surface area contributes to the measured signal, therefore averaging effect occurs which lowers the resolution [44]. Also, KPFM is very sensitive to the exact surface conditions, for example humidity [51]. The exact determination of work function is then not straightforward at all.

3.3. Applications of KPFM

The purpose of this section is to outline the variety of applications KPFM can be utilized for. KPFM is very versatile tool, although, it is often difficult to correctly interpret the measurements and to avoid some of the errors, as mentioned in the last part of previous section. KPFM can be used to study local electronic properties with nanometer resolution, in special cases even up to molecular and atomic resolution (as reviewed in [49]). However, in my opinion, the biggest advantage of KPFM is that the measurements can be carried out on working devices in real operation conditions. The KPFM measurements can be also supported with other complementary techniques based on the AFM [46]. Stronger emphasis will be put on the applications related to the 1D nanostructures and photoelectrochemistry (photoassisted KPFM).

A special section devoted to the applications of PES is omitted, because the principle of the most common applications is rather straightforward (the measurement, however, can be very difficult to carry out and to interpret properly). XPS is mainly used to study the chemical composition and UPS to determine the work function and to study the valence band states. More advanced angle-resolved modifications of those methods allow the study of layer thickness (angle-resolved XPS) or detailed valence band structure (angle-resolved UPS).

3.3.1. Applications of standard and high resolution KPFM

As reviewed in [49], KPFM can find applications in analysis of many different materials. This section is a brief overview of some of the possible applications presented in this review to create a general picture of how KPFM can be used.

Starting for example with metallic nanostructures, which can be used for instance for heterogenous catalysis or in sensors, KPFM can provide insight into the charge transfer between the nanostructures and surfaces (catalysis) or nanostructures and adsorbed molecules (sensors). Valuable information extracted by the KPFM can be also for example the size dependency of the work function of the nanostructures or visualisation of charged defects, which can play significant role during e.g. nanostructure growth or adstorption of molecules.

Considering the semiconductor surfaces, high resolution KPFM has been already utilized to image surface defects and adsorbed molecules. Also imaging the surface reconstruction and the identification of individual atoms has been performed with the combination of noncontact AFM and KPFM, thanks to the ability of noncontact AFM to achieve atomic resolution and to the fact that different atoms exhibit different surface potential measured by KPFM. However, it is important to note that achieving atomic resolution require special conditions and is always very challenging. (Mainly because of the need for a very sharp tip, the need for measuring very small forces while avoiding the the noise and external vibrations, the need for isolating the detection of short range repulsive forces from long range attractive forces (finding optimal cantilever and scanning parameters etc.) and avoiding additional obstacles such as jump-to-contact caused by attractive forces. Atomic resolution AFM is mostly performed in the noncontact frequency modulation mode [48].

Another large field of the applications of KPFM is in the characterization of electrical properties of devices. For example charging states of quantum dots can be observed by the change in their surface potential. The charging of individual quantum dots can also be achieved by applying a voltage on the tip.

Very important has been the possibility to image potential profiles in semiconductor junctions, allowing for example the visualisation of the p-n junction under working conditions. KPFM can be also used for identifying the features responsible for a decrease in device performance, such as high contact resistance caused by Schottky barriers in field effect transistors. With cleaved samples, KPFM can provide information about doping profiles.

KPFM on nanowires

Apart from the applications mentioned above, KPFM has been already used to study 1D nanostructures as well. With the utilization of the KPFM measurements on sin-

gle nanowire (NW) device and with comparison with a model, several characteristics of the nanowire can be extracted such as surface states density, doping distribution or measurement of trap states.

Halpern et al. have used KPFM to examine the surface states in single InAs nanowire. They fabricated nanowire field effect transistor (FET) device and measured the surface potential while changing the back gate voltage (fig. 3.10). Both source drain electrodes were grounded. With the help of 3D electrostatic simulation, they were able to extract the surface states concentration and their energy distribution.

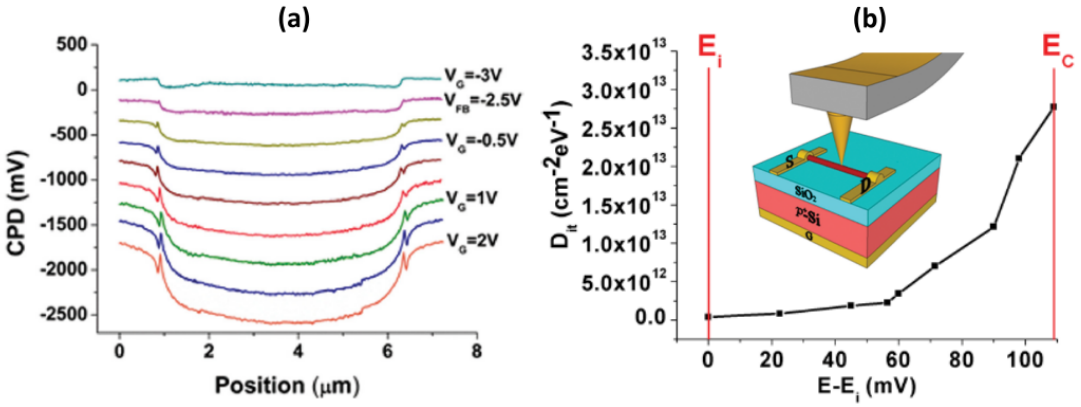

Fig. 3.10: *KPFM analysis of surface states by Halpern et al. (a) CPD measured along single nanowire FET device for different back gate voltages. (b) Extracted energy distribution of surface states. The inset shows a model of the actual device under measurement. Adopted from [52].*

Koren et al. [53] have analyzed the doping distribution along single doped Si nanowire by KPFM and correlated it with Scanning Photocurrent Microscopy (SPCM). They had the nanowire contacted from both sides and measured the current flow through the NW while simultaneously measuring the surface potential by KPFM. From the longitudinal distribution of surface potential they calculated the electric field as $E(x) = \frac{\partial V_{\mathrm{CPD}}}{\partial x}$ and then extracted the dopant distribution according to $j(x) = \sigma E(x) = e\mu N_{\mathrm{D}} E(x)$, where $j(x)$ is the current density, σ is the conductivity and e elementary charge. The carrier mobility μ was expected to be constant and the same as in bulk under an assumption that due to high doping, the surface potential is a good approximation of the bulk potential.

Koren et al. have also analyzed the radial active dopant concentration in doped sillicon nanowires [54]. They have achieved this by sequential selective etching of the nanowire using masks with different sizes so they created a nanowire where different parts had different diameter. Next, they compared the surface potential of parts with different diameters with a model and they could evaluate the radial doping density and the current density when the device was under operation. They also managed to image the trap states in nanowires using the NW FET device with grounded source and drain electrodes [55]. When bias was applied to the back gate electrode, they observed "dips" in the potential profile along the nanowire and evaluated the nature of the trap states (i.e. acceptor-like or donor-like). Again comparing the experiments with a model, they managed to extract the trap state energy with respect to the conduction band.

As presented above, Si nanowires have been already extensively studied. However, other 1D nanostructures can have also promising applications and it is important to deeply analyze them to be able to tune the nanostructure properties for potential devices. Taking

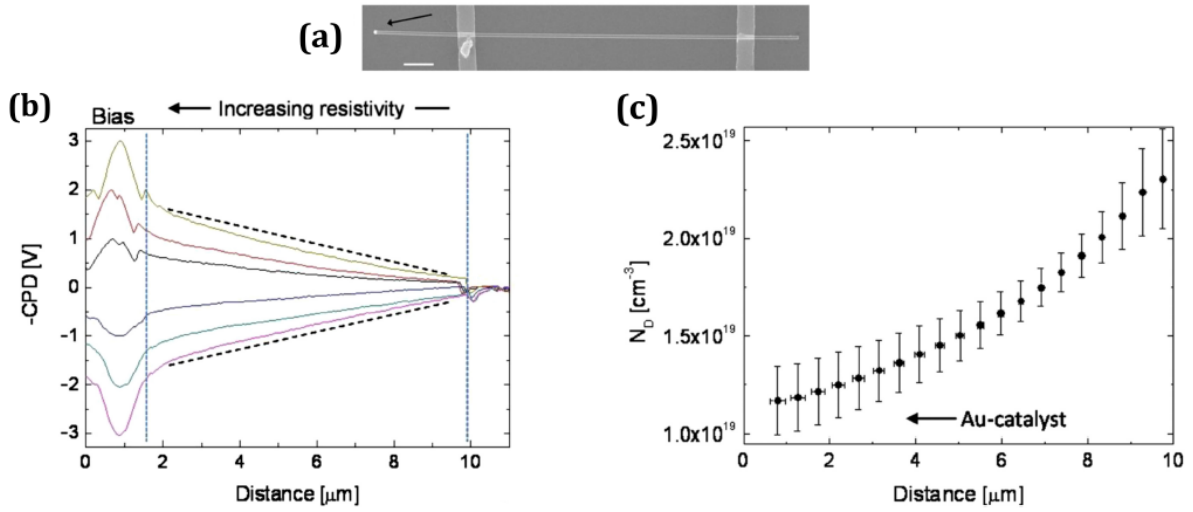

Fig. 3.11: *Analysis of longitudinal doping distribution by Koren et al. (a) SEM image of the measured nanowire device, (b) CPD profiles along the NW when different bias is applied to one of the electrodes. (c) Extracted longitudinal doping concentration profile. Adopted from [53]*

into account the presented examples, KPFM can provide a lot of useful information about surface and electronic properties.

3.3.2. Photoassisted KPFM

Kelvin Probe Fore Microscopy is also an excellent tool to study local properties of materials under illumination. This can be especially useful when analyzing solar cells or photocatalyst materials. When the difference of the surface potential in the dark state and illuminated state is measured, one can for example obtain some information about the photogenerated charge transport or surface band bending. With some advanced analysis techniques, it is also possible to evaluate the charge carrier lifetime or diffusion length [56]. Since the KPFM is used together with external light illumination, it is often named "Photoassisted KPFM".

Photoassisted KPFM actually utilizes the so called Surface Photovoltage (SPV) phenomenon. SPV has been already studied since the late 1940s and have become important tool to characterize semiconductors, especially for solar cell applications. Both theory and applications of SPV are quite in detail described in L. Kronik's review from 1999 [56]. Since the development of KPFM, the surface photovoltage has been possible to study even in nanostructures with much increased resolution.

In short, the SPV measurement is the detection of changes in surface potential under illumination, when the sample with a back contact is grounded. The absorbed photons can either create electron-hole pair if the energy of the photon is higher than the band gap (super-bandgap illumination), or released trapped charge carriers from trap to bands when the energy of the photon is lower than the band gap (sub-bandgap illumination). These released charge carriers can be transferred from the surface to the bulk or vice versa, rearranging the charge distribution and causing the change in the surface potential.

In the simplest case, SPV measurements can be used to approximately determine the band gap of the material as well as the type of semiconductor (according to the sign

of the photovoltage) [56]. This method is actually analogous to the absorption spectroscopy and sometimes called Surface Photovoltage Spectroscopy (SPS). When the sample is illuminated by monochromatic light with variable wavelength, a large change in the SPV is expected when the energy of the light matches that of the band gap. The advantage over transmission spectroscopy is that the sample does not have to be transparent.

The fact that SPS is sensitive to the surface, in-gap surface states may on one hand hinder the determination of a band gap, but on the other hand it allows to actually probe and study those surface states when the sample is exposed to sub-bandgap illumination [56].

More advanced approaches allow to obtain information about the minority carrier diffusion length and band bending [56]. The value of minority carrier diffusion lenght can be reached by illuminating the sample with different intensity and plotting the ligth intensity versus the inverse absorption coefficient for a constant achieved photovoltage value. With linear interpolation of the data, the intersection with the inverse absorption coefficient axis yields the diffusion length. The principle of achieving the magnitude of surface band bending is based on the fact that super-bandgap illumination with sufficient intensity should completely flatten the bands, therefore if the SPV is measured as a function of illumination intensity, saturation should be possible to reach and the SPV in this saturation regime is equal to the surface band bending with opposite sign. This should be theoretically always possible, however, the high intensity illumination (and heating) can induce irreversible changes in the surface physical properties.

In more recent works, there were also attempts to extract minority carrier lifetime from KPFM measurements [57]. For this purpose, time dependence of the surface potential has to be measured. The feedback system of the KPFM is, however, relatively slow (greater than miliseconds [58]), but this obstacle can be overcome by several methods. For example, with the use of pulsed illumination with frequency greater than the KPFM feedback bandwidth, KPFM yields an average surface potential [58].

Takihara et al. presented a method on how to evaluate the carrier lifetime in Si solar cell while measuring the average photovoltage under pulsed illumination with variable frequency [57]. They compared the average potential with a model based on the assumption that the photovoltage rises abruptly to a steady state right after illumination. Meanwhile, it returns back to zero in different manner when the illumination stops due to different recombination processes. They expected the surface recombination to be very fast (due to a presence of surface states) and the bulk recombination slower. The photovoltage decay follows exponential dependence and the time-average of the photovoltage can be calculated as (fig. 3.12)

$$V_{\mathrm{av}} = \frac{V_{\mathrm{max}}}{T}\left\{\int_0^{T/2} dt + \int_{T/2}^{T}(1-r)e^{-(t-T/2)/\tau_{\mathrm{b}}}dt\right\}, \tag{3.11}$$

where V_{max} is the photovoltage under continuous illumination, T is the period of the illumination, r represents the contribution of the surface layer to the photovoltage and τ_{b} is the minority carrier lifetime in the bulk. Then, the time-averaged photovoltage is measured as a function of pulsed illumination frequency and the experimental data are fitted with the model, which allows to determine the constants in the model, including the carrier lifetime.

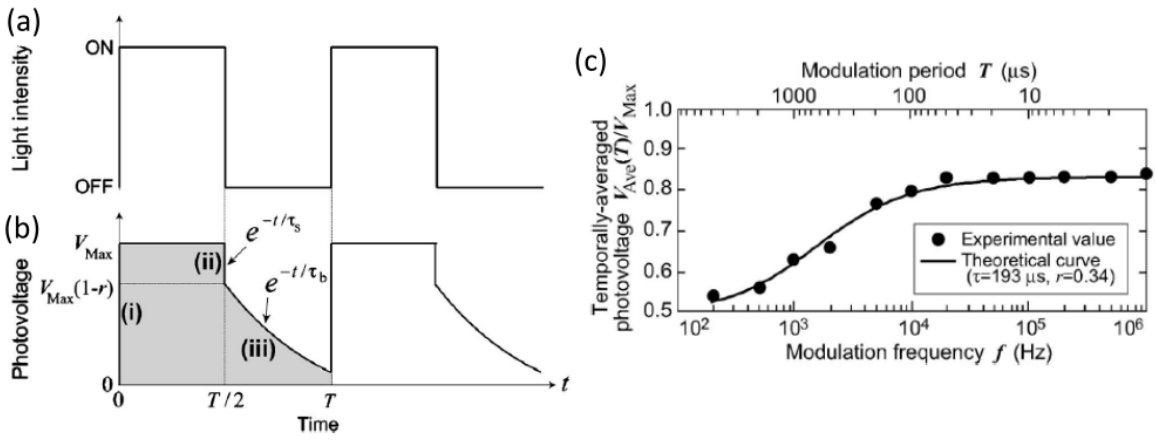

Fig. 3.12: *Analysis of minority carrier lifetime with KPFM and pulsed illumination by Takihara et al. (a) Light pulse profile and (b) modelled time dependency of the photovoltage. (c) Time-averaged photovoltage measured under pulsed illumination with different frequency by KPFM. The experimental data is fitted with theoretical curve calculated as time-averaged photovoltage according to the model in (b), which allows the determination of carrier lifetime.*

More recently, more analyzing techniques were developed to study charge dynamics under pulsed illumination with KPFM. For example, Schumacher et al. achieved much higher accuracy using gated integration method, recovering the CPD from the frequency shift of the oscillations of the tip in time domain [58]. Giridharagopal et al. utilized big data capture and recorded the cantilever deflection versus AC voltage multiple times within a single cantilever oscillation and extracted the CPD value with sub-milisecond resolution [59].

Photoassisted KPFM on 1D nanostructures

Photoassisted KPFM with relation to the 1D nanostructures have found its use mainly to study charge transfer and charge dynamics, mainly in the field of solar cells and photocatalysis. Liu et al. used KPFM to study the role of single wall carbon nanotubes introduced into organic solar cells [60]. They found out that introducing nanotubes into the organic layer increases the mobility of holes. Lan et al. studied carbon nanotubes in organic solar cells [61]. With the help of KPFM, they explained the improved performance of cells with nanotubes. They constructed the band structure diagram and realized, that carbon nanotubes act as a channel for holes while blocking electrons.

As already mentioned, KPFM has also found its use when studying photocatalytic materials. For example, Lin et al. have studied SnS_2 nanosheet/TiO_2 nanotube interface used for photoelectrochemical water splitting [62]. They used KPFM as complementary technique to the photocurrent measurement, Tauc plot [28] and Mott-Schottky plot [63]. They again managed to construct the band diagram and revealed that their device with hydrogenated TiO_2 nanotubes has improved performance due to better band alignment and due to the existence of in-gap states near the nanotube conduction band. Another work presented by Liu et al. is a study of core-shell semiconductor nanowires (Si/TiO_2) for water splitting [64]. They again used the KPFM to study the band alignment and charge transfer under illumination. The core-shell nanowires allow to have both broad

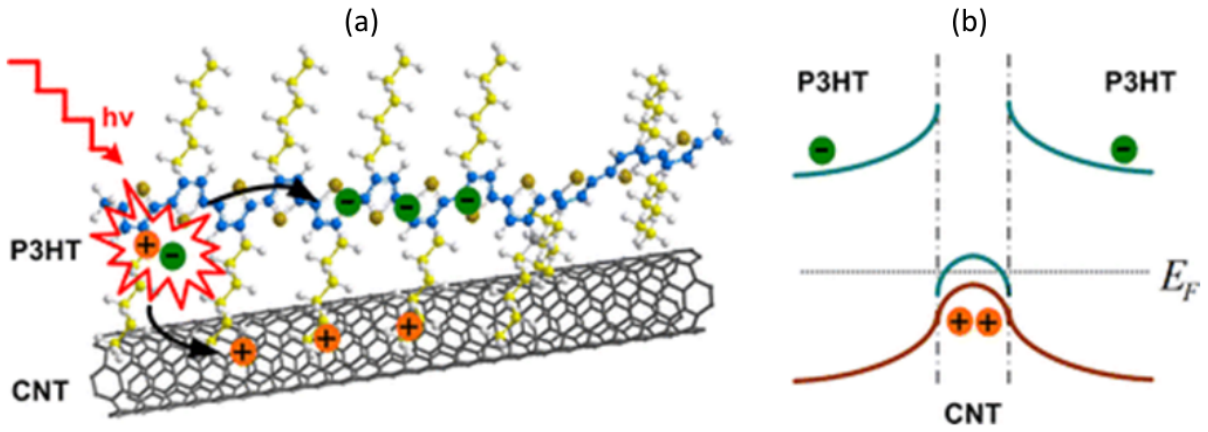

Fig. 3.13: *Analyzing carbon nanotubes (CNT) in organic solar cells (P3HT - the organic polymer layer) by Li et al. With the help of KPFM, they constructed the (b) band diagram and figured out (a) that the nanotube acts as a channel for holes while electrons are blocked and kept in the polymer. Adopted from [61]*

band absorption (Si core) and suitable band edges for efficient oxidation/reduction and charge transfer (TiO_2 shell). Yoo et al. tried to modify TiO_2 nanotubes, particularly with gold nanoparticles, and revealed how the charge transfers under illumination with KPFM [65]

Photoassisted KPFM was also used to study the surface states on $BiFeO_3$ nanowires [66] by sub-bandgap illumination or even imaging the plasmon field enhancement around metal nanoparticles under illumination [67].

As a conclusion to this section, KPFM has a very wide variety of applications ranging from mapping the work function differences and detecting different elements on the surface to advanced analysis of material properties and charge transfer/dynamics, all with the resolution in range of nanometers. Its best use seems to be as a complementary technique to other optical/electrical analyzing methods, with the biggest advantage that the measurements can be performed in real operating conditions of the studied devices.

4. Experimental part

The motivation of the thesis was to follow on experiments of Ing. Filip Ligmajer, PhD. In his dissertation thesis [3], he presented an experiment where he tried to use novel electrode materials. He observed different photoelectrochemical activity when diverse electrodes were used. He used Indium Tin Oxide (ITO) electrodes with tungsten disulfide nanotubes (WS_2 NTs) which were either bare or decorated with Au nanoparticles. He explained his results by schematic band diagrams similar to that shown in chapter 1.1. To construct those band diagrams, material values from literature were used. Now, the purpose of this study is to evaluate some of the material characteristics of the actual materials used in his experiments (the same kind of ITO electrodes and WS_2 nanotubes from the same supplier).

In particular, the main goal of this experimental part was to measure the work function and the position of the valence band edge with respect to the Fermi level of the materials used in F. Ligmajer's experiments (ITO and mainly WS_2 nanotubes). For this task, Ultraviolet Photoelectron Spectroscopy (UPS) and Kelvin Probe Force Microscopy (KPFM) were used. UPS is a common tool used to study the valence band structure and also the work function. The measurements have to be performed in Ultra High Vacuum (UHV). Compared to the UPS, KPFM measures only the contact potential difference, which is related to the work function and not to the valence band structure. However, the KPFM measurements can be performed in ambient conditions, and therefore it should be interesting to compare the results.

The X-ray Photoelectron Spectroscopy (XPS) measurements were also used a lot as they can be performed on the same instrument as the UPS and provides valuable information about the chemical composition of the sample. It was used mainly to detect the amount of adventitious carbon contamination, the amount of WS_2 nanotubes on the surface and to detect possible changes or damage to the sample when different treatments were used.

4.1. Experimental details

The XPS and UPS measurements were performed on an AXIS Supra photoelectron spectrometer from Kratos Analytical Ltd. at the CEITEC Nano research infrastructure. The instrument provided a monochromatic Al K_α radiation (1486.6 eV, with Rowland circle monochromator). The analyzer extraction axis was perpendicular to the sample surface[1] and the angle between the source and the analyzer was the so-called "Magic angle" ($\sim$54,7°). This instrument also provides a possibility to heat the sample with a special heating stage up to about 800 °C and to sputter the sample surface with Ar^+ ions or clusters with variable energy. For the UPS measurements, standard He discharge lamp is provided (He I line of 21.12 eV).

The KPFM measurements for work function comparison were performed in ambient conditions on a Dimension ICON AFM from Bruker at the CEITEC nano research infrastructure. The standard Bruker SCM-PIT tips for electrical measurements were used

[1] All measurements were performed in this setup. However, the instrument provides also the possibility to tilt the sample to perform angle-resolved measurements.

(PtIr coated). The topography was acquired in peak force tapping mode, and the KPFM in second pass in amplitude modulation mode.

The commercial ITO Samples were from Delta Technologies (∼120-160 nm thick ITO layer on a glass substrate) with sheat resistance of 5-15 Ω/sq.

The samples with WS_2 nanotubes were prepared for the measurement using following procedure. The nanotubes in a powder form (provided by R. Tenne from Weizmann Institute of Science, Israel) were dispersed in a solvent (e.g. IPA, cyclohexane or water). Sufficient separation of the nanotubes from each other was achieved by several (5-7) three minute cycles in ultrasound, and the solution was always shook in hand in between the cycles. Subsequently, the solution was drop-casted onto a desired substrate and let dry naturally. Eventually, the substrate was heated to speed up the drying process.

4.1.1. Evaluation of the UPS spectra

The principle of UPS and the method of evaluation of the work function and the valence band position was already described in section 3.1.3 and in Fig. 3.7. This can be used for homogeneous materials.

The particular method how to determine the work function from the spectrum is showed in Fig. 4.1. Several points in the spectrum corresponding to the highest derivative are selected. Those points are fitted with linear function and the work function is determined as the intersection of this linear fit with zero counts line. The uncertainty of this approach was considered as 0.12 eV, which is the declared resolution of the instrument analyzer.

The valence band position with respect to the Fermi level ($E_F - E_v$) was extracted with similar approach (Fig. 4.2). The difference is that the region for fitting was selected manually. In this case, the slope of the fit is smaller and the particular selection of the points to fit have higher influence on the calculated intersection with zero. Because of that, the uncertainty of the $E_F - E_v$ was usually considered slightly higher (in range of 0.13 to 0.14 eV) when different choices of the points to fit were considered.

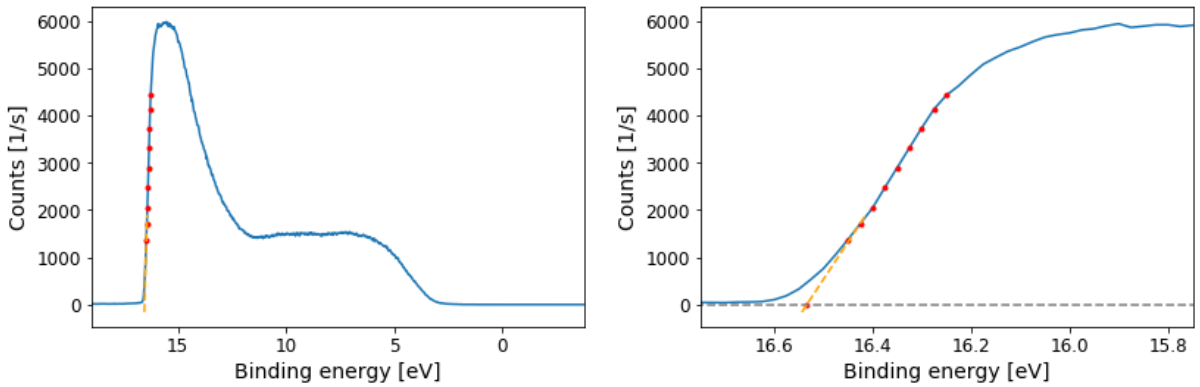

Fig. 4.1: *Extraction of the work function from UPS spectrum. The whole spectrum (left) and a detail of the work function edge (right). The work function edge was fitted by linear function in a region of highest derivative. The root of the linear function is used to calculate the work function according to eq. 3.3.*

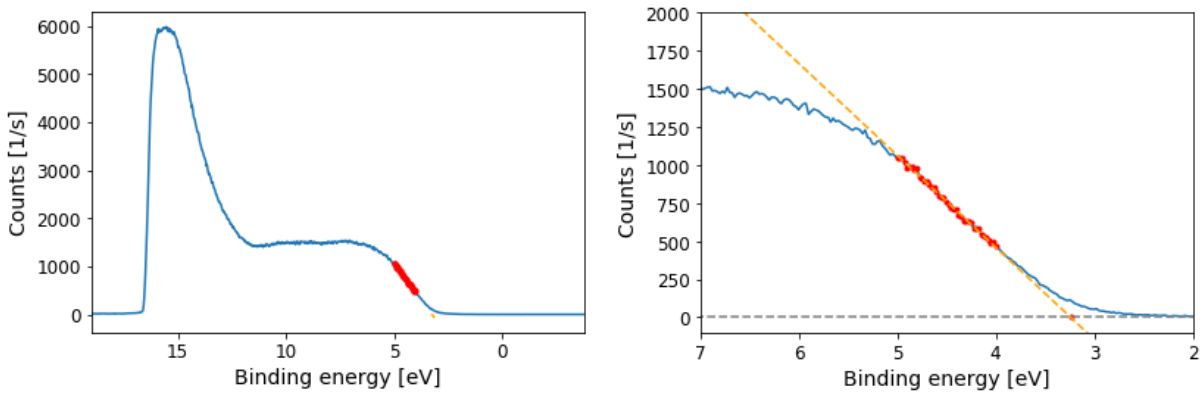

Fig. 4.2: *Extraction of the $E_F - E_v$ from an UPS spectrum. (left) the whole spectrum and (right) detail of the valence band edge region. The valence band edge was fitted by linear function in a region of highest derivative. The root of the linear function is $E_F - E_v$ value.*

4.1.2. Difficulties in the UPS measurement

In order to avoid significant error in the measured spectra, the sample should be conductive. This demand arises from the fact that the photoelectrons and Auger electrons leave behind a positive charge when emitted, leading to a charging of the surface. If the sample is conductive enough, the electrons from bulk balance this build-up of charge on the surface. In other case, the whole spectrum can be shifted due to this charging effect, leading to incorrect work function and valence band edge position extraction from the spectrum. Fortunately, the materials that are a subject of this study are conductive.

Considering the shift of the spectrum, an unwanted effect was sometimes observed in the measurements. When consecutive UPS mesurements were performed, the spectrum had shifted to higher binding energies (BE) after each subsequent measurement (fig. 4.3a). This effect was attributed to the surface contaminant layer (charging or perhaps some different change) because this effect was much less pronounced if a sputtering of the sample was performed before UPS measurement. For that reason, I tried to avoid or remove the surface contaminants (adventitious carbon, organic remains from sample pre-treatment) by in-situ sputtering or choosing different sample pre-treatment.

The reason for eliminating the surface contamination is also the fact that UPS is a very surface sensitive, so any surface contamination could make the measured spectrum appear completely different. As an example, in the spectrum of the non-sputtered gold with adventitious carbon contamination, it is not possible to see the valence band peaks. Additionally, the signal at Fermi level is very low compared to the spectrum of the sputtered gold (Fig. 4.3b). From the fact that at the 0-1 eV region the signal is almost zero, I judge that the adventitious carbon layer completely covers the surface and also effectively shields the gold so no electrons from gold are detected. Thus, the signal comes mainly from the surface contamination layer (otherwise the Fermi edge at zero binding energy would have been visible in the spectrum).

Another effect that was observed was a difference between the UPS spectrum measured right after inserting the sample in the analysis chamber and the UPS spectrum obtained after an XPS analysis. This might also be due to charging of the surface or due to some other change in the surface layer caused by the X-ray irradiation (Fig. 4.4).

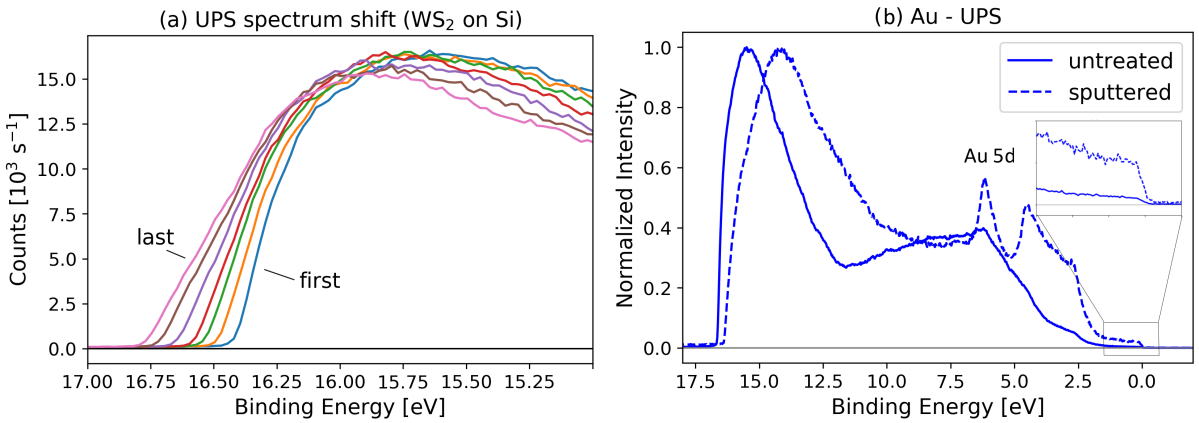

Fig. 4.3: *(a) An example of the change in the spectrum after successive UPS measurements (all measured within ∼20 min). This effect is attributed to some changes or charging of the surface contaminant layer. (b) Effect of sputtering on the UPS spectrum of gold. Before sputtering, the surface is covered with surface contaminants so the valence bands are not visible and the signal at the Fermi level position is very low.*

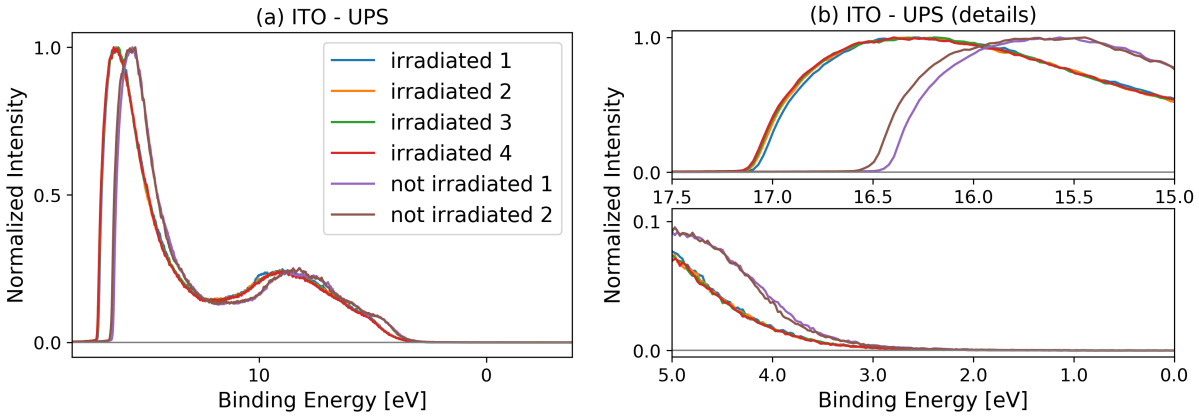

Fig. 4.4: *The effect of XPS measurement on UPS spectrum (ITO, no previous treatment). Irradiation with X-rays during XPS measurement (∼20 min) causes a shift of the spectrum to higher binding energies. (a) the whole UPS spectra and (b) details of the same spectra – the work function changes by more than 0.5 eV upon irradiation and also the valence band edge is different. This effect is attributed to some changes or charging of the surface contaminant layer.*

Due to the above mentioned effects, the samples in the following experiments were measured by UPS before any other measurements in order to avoid possible changes and charging due to additional irradiation. The measurement stability was considered sufficient when 4 consecutively measured spectra shifted significantly less than the declared analyzer resolution (0.12 eV).

Additionally, the samples were sputtered in order to remove the surface contamination, if possible. However, this could only be used when "bulk" homogeneous material properties were analyzed (Gold or the Sn:In_2O_3 of the ITO). However, considering the use in electrochemistry, it is the surface that takes part in the reactions. In that case, sputtering might also change or damage the surface layer (it will be later discussed that the ITO

surface changes with different sample treatment [68]). Hence, this indicates that the UPS analysis is not straightforward at all.

4.1.3. Evaluation of the KPFM images

The KPFM images used to analyze the work function in the next section (4.2.3) were taken within a single measurement day with the same tip. An example of such an image is shown in Fig. 4.5. The CPD used to calculate the work function was determined as a modus of all values in the KPFM image.

The uncertainty of such CPD determination was estimated from a histogram of the CPD values within the KPFM image as the half peak width in ∼1/10 of its height, ignoring the tails of the distribution (Fig. 4.6).

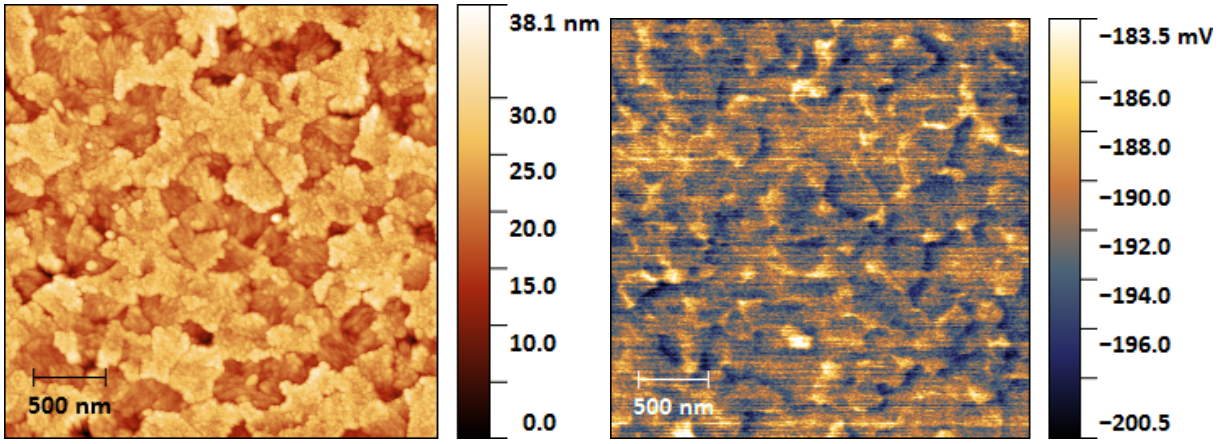

Fig. 4.5: *An example of topography (left) and KPFM image (right) of an ITO sample. The CPD used to determine the work function was calculated as a modus of all values in the KPFM image.*

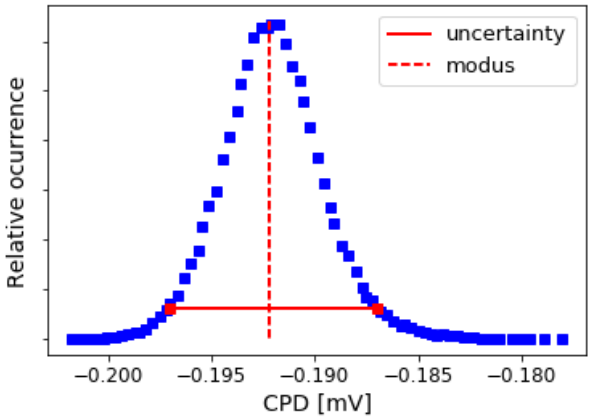

Fig. 4.6: *Determination of modus CPD value and its uncertainty from histogram of values extracted from KPFM image.*

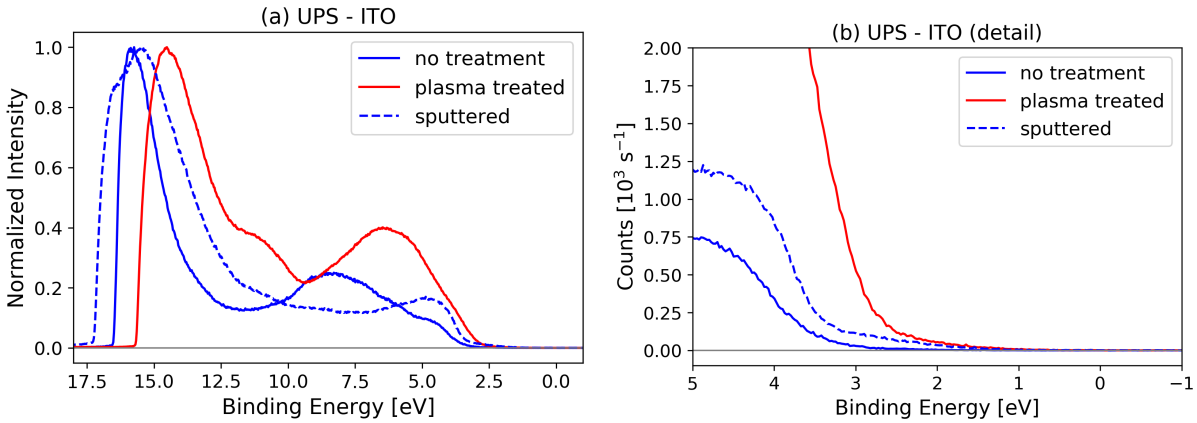

Fig. 4.7: *A comparison of UPS measurements on differently treated ITO samples. (a) Whole spectrum and (b) a detail of the region at the valence band edge.*

4.2. Indium Tin Oxide

Theoretically, extracting the work function of the Indium Tin Oxide (ITO) from UPS spectrum should be simple. However, because of the fact that UPS is very surface sensitive, the work function extracted from the spectra differed substantially depending on the sample treatment and history. For that reason, more detailed analysis of the influence of the sample treatment on the surface and its relation to the work function was analyzed. In order to obtain more information, XPS analysis was also used for this purpose.

4.2.1. Effect of sputtering and plasma cleaning

In order to analyze the effect of sputtering and plasma treatment, two ITO samples were compared. One was in-situ sputtered and the other was ex-situ treated by O_2/Ar plasma for 1 minute. The plasma treated sample was inserted to the vacuum and analyzed within an hour after the plasma process. As shown in Fig. 4.7, both the work function and the valence band position differs substantially depending on the treatment. The extracted values are presented in Table 4.1. The properties of untreated sample are probably highly affected by adventitious contamination while the properties of sputtered sample should be corresponding to the bulk Sn doped In_2O_3. A work function increase was also reported after in-situ plasma treatment by Ishii et al. [69]. The work function measured after plasma treatment was lower (5.41 eV) compared to the value measured by Ishii (∼6.0 eV) probably due to a short exposure to air and the little amount of adventitious carbon adsorbed on the surface.

The plasma cleaning probably changes only the properties of the very surface, because according to XPS measurement (which integrates the signal from ∼10 nm depth),

Table 4.1: *Measured values of work function ϕ and valence band position with respect to Fermi level $E_F - E_v$ of differently treated ITO samples.*

	ϕ [eV]	$E_F - E_v$ [eV]
no treatment	4.72 ± 0.07	3.50 ± 0.08
sputtering	3.95 ± 0.07	3.32 ± 0.08
plasma	5.41 ± 0.07	2.99 ± 0.08

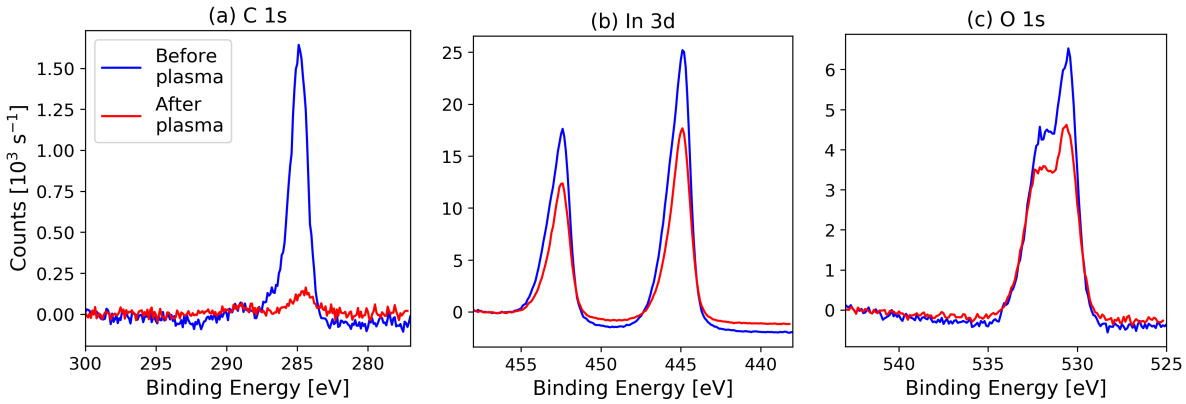

Fig. 4.8: *XPS spectra of an (a) C 1s, (b) In 3d and (c) O 1s peak of an ITO sample before and after plasma treatment. Carbon was removed effectively and no other chemical change was observed.*

no change in the chemical composition was observed, only carbon contamination was removed quite effectively (Fig. 4.8). A slight change in total signal intensity is visible in the spectrum. This is probably due to the reduced amount of carbon contamination leading to higher signal from the ITO.

4.2.2. Modifying the surface with during deposition process

Since ITO is used as substrate for the WS_2 nanotubes in electrochemical experiments, the deposition of nanotubes might also have an impact on the ITO surface properties. The nanotubes are usually dropcasted onto an ITO from a solution (Acetone, Isopropyl Alcohol, water, etc.). When analyzing the nanotubes (described in the next section 4.3), it was noticed that the ITO substrate can be modified. In particular, this happened when the nanotubes were deposited from water and the solution was drying several hours on the sample.

When In 3d peak is examined (Fig. 4.9), there is a difference between a regular untreated sample and a sample with WS_2 nanotubes deposited from water. The In 3d peak of an untreated sample can be deconvoluted into a main In_2O_3 compound peak and an additional peak which might possibly correspond to an In atom close to O vacancy (similar to an O close to O vacancy observed in [68], but it should be noted that proper identification of the origin of all the peak compounds would require deeper analysis, which was not a goal of this thesis). The In 3d spectral region of a sample with NTs deposited from water has an additional peak in the spectrum that probably corresponds to an InOOH or $In(OH)_3$ compounds that can be formed on the surface [68]. The last unlabeled peak is there for improved fitting and its origin is unknown.

Hence, a main conclusion from this part is that water treatment can modify the ITO surface by forming $InOOH/In(OH)_3$, which can lead to a change in the electronic properties of an ITO-nanotube interface. It was also observed that when the sample was heated during the deposition, the solution droplet dried faster (minutes) on the sample and such strong effect of oxy- and hydroxy- compounds formation was not observed. However, in another experiments where pure water droplets were drop casted onto the samples, the effect was not observed. This includes both depositions at room temperature (slow drying) and elevated temperature (fast drying) at both plasma treated and untreated

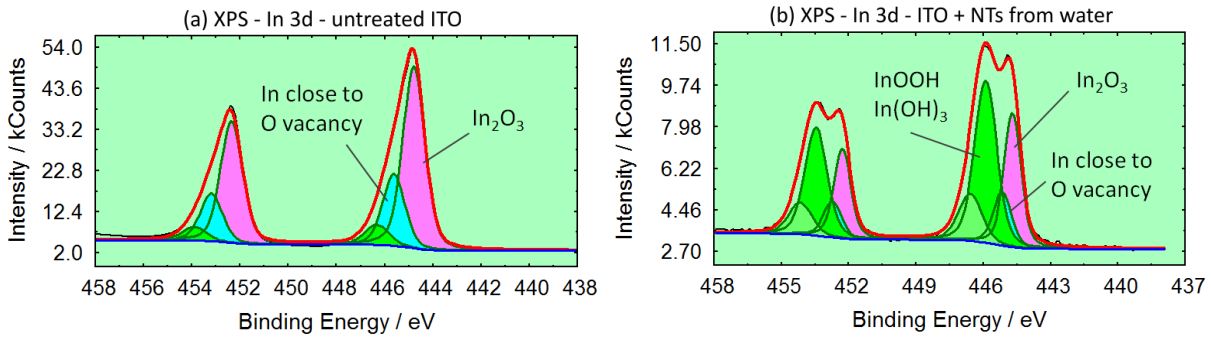

Fig. 4.9: *Deconvolution of In 3d peak of (a) untreated ITO and (b) ITO with WS_2 NTs deposited from water. The NTs solution droplet was drying several hours on the sample. An additional peak corresponding to InOOH/In(OH)$_3$ compounds is visible. Charge reference: C 1s – 284.8 eV.*

ITO substrates. So there is also a possibility that the InOOH/In(OH)$_3$ modification was caused by possible previous water/humidity exposure to the sample or the water solution with nanotubes acts differently than pure water.

Unfortunately, this observation was made in rather later stage of the work so there was not enough time to study this effect deeper however interesting it may be.

4.2.3. Effect of different solvents used for the NTs deposition

In order to test the effect of the treatments used for NTs deposition, seven differently treated samples were prepared – as recieved, plasma cleaned and exposed to water/IPA (Isopropyl Alcohol) with different combinations. The reason why such sample treatments were chosen is that when the ITO electrode is prepared for electrochemical experiments, the sample can experience similar environment. (When the ITO electrode is decorated with nanotubes, the nanotubes are drop-casted from an aqueous or IPA solution. Also the electrochemical experiments are usually performed in aqueous solution.)

On all samples except the untreated one, a 25 nm layer of gold was sputter-deposited onto a part of the sample to provide work function reference for subsequent KPFM measurements (a ∼3 mm stripe on one side of the sample, the other part of the sample was covered by parafilm tape during the depositions). The plasma treatment was performed by O_2/Ar plasma for 1 min. The solvents were drop-casted either at room temperature and let dry slowly or at elevated temperature (substrate temp. 80 °C). The IPA drop-casted onto the ITO part of the sample always affected also the Au reference layer due to good wettability whereas the water droplets stayed on the ITO part due to higher hydrophobicity of the ITO. The samples and their treatments in chronological order are listed in Table 4.2.

The samples were first measured by UPS, then by XPS right after and, lastly, a KPFM measurement was performed at last. Since the KPFM is a relative measurement technique, a reference sample is needed for the work function determination if the work function of the tip is not known. For this purpose, the Au layer deposited onto a part of each ITO sample was used. The work function of gold measured by UPS on each sample was used to calculate the work function of the tip and then the work function of the tip was used

Table 4.2: *Different treatments of tested ITO samples*

sample	treatment
no. 1	as recieved
no. 2	parafilm (Au dep.), plasma, IPA (80 °C)
no. 3	parafilm (Au dep.), plasma, H_2O (80 °C)
no. 4	parafilm (Au dep.), plasma, IPA
no. 5	parafilm (Au dep.), plasma, H_2O
no. 6	parafilm (Au dep.), IPA
no. 7	parafilm (Au dep.), H_2O

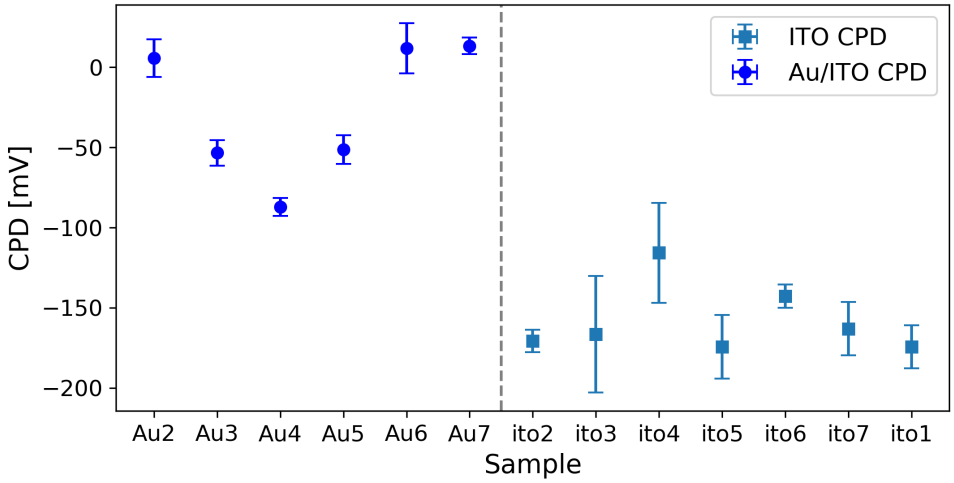

Fig. 4.10: *CPD measured on all samples described in Tab. 4.2. The CPD measured on ITO is more negative compared to Au, corresponding to lower work function of ITO (measured with PtIr coated tip).*

.

to determine the work function of ITO (both according to equation 3.6). The KPFM measurements were carried 4 days after the UPS and XPS measurements.

The CPD measured by KPFM is shown in Fig. 4.10. The presented values are always an average of two measurements at different spots on the sample, and the error bars are calculated as a combined error of standard deviation of the two measurements and the error of single measurement described in section 4.1.3. The CPD of ITO is more negative, which corresponds to lower work function as expected.

Fig. 4.11 presents the work functions of all samples analyzed by UPS plus work functions of ITO samples calculated from KPFM measurements. The work functions of ITO samples were always calculated using the Au reference on the same sample (Au2 was used for the ito1 untreated sample as a reference since it did not have its own Au layer reference). The errors of the UPS measurements is determined by the instrument resolution of 0.12 eV divided by $\sqrt{3}$ since the spectra were averaged over three individual sweeps.

The work functions of ITO determined by KPFM are generally higher than the work functions determined by UPS. This difference is caused by the fact that the UPS measurements are performed in vacuum and KPFM in ambient conditions. In ambient conditions, additional adsorbed molecules (mainly water) change the work function of the surface. This change of work function has different magnitude for Au and ITO, which causes the values determined by KPFM to be higher.

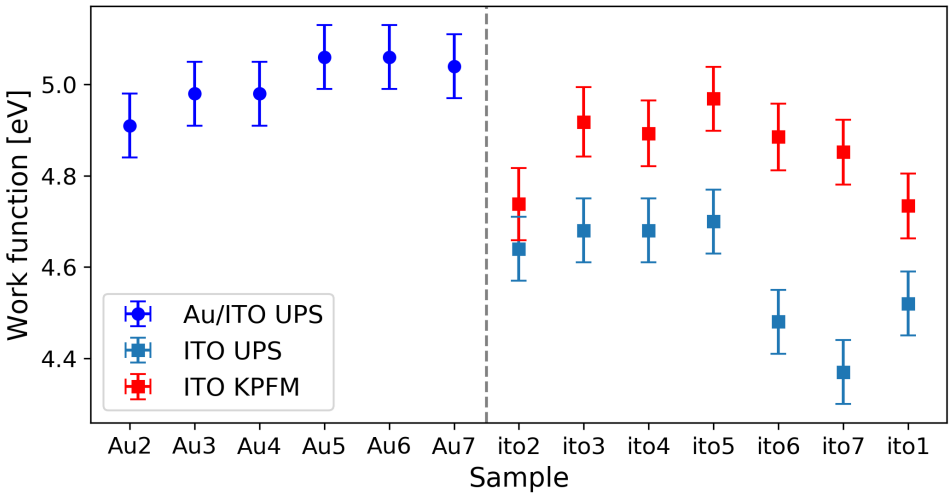

Fig. 4.11: *Work function of all samples described in Tab. 4.2. The work functions determined by KPFM were calculated using the gold stripe on each sample as a reference. Sample ito1 did not have a gold stripe reference so previously measured gold sample was used (Au2). The KPFM values differ from the UPS values because the KPFM measurements were performed in ambient condition.*

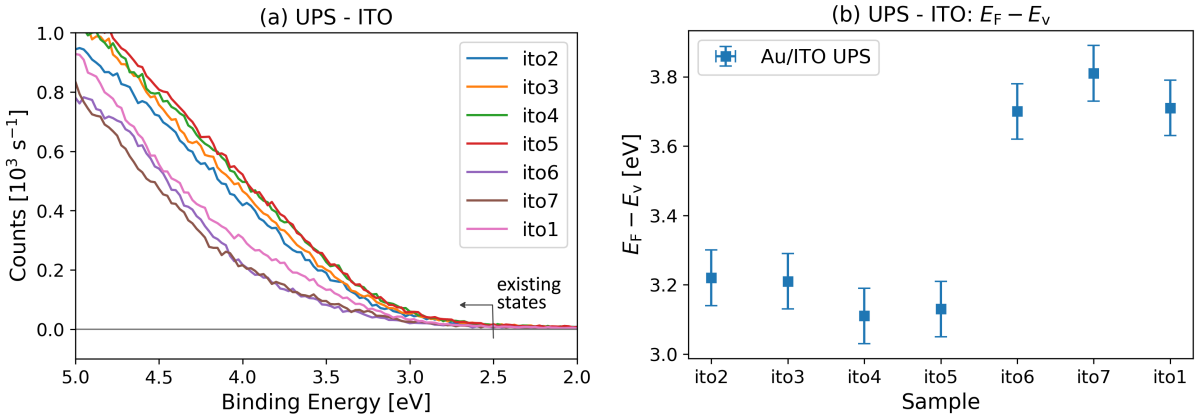

Fig. 4.12: *(a) Detail of the valence band edge measured by UPS and (b) $E_F - E_v$ determined by linear fitting described in section 4.1.1. The $E_F - E_v$ is by ∼0.6 eV lower for samples that were plasma treated. However, there are some states visible from 2.5 eV. on both samples.*

Considering the work functions of Au determined by UPS, it is difficult to figure out some trend. If we look at the plasma cleaned samples (Au1 - Au5), the IPA treated samples (Au2, Au4) seem to exhibit slightly lower work function (∼0.1 eV) compared to their water treated counterparts. The plasma cleaned samples seem to rather higher work function. These results are in agreement with expected values, the additional carbon contamination that can be brought from IPA might lower the work function, because when a sputtered gold was measured, an increase in work function was always observed. However, no significant differences in the C 1s peak intensity were detected by XPS. Overall, the work function of Au does not vary by more than 0.2 eV among the samples.

Considering the ITO, one trend in the UPS measurements is visible. The plasma cleaned samples (ito2 - ito5) exhibit higher work function (by ∼0.2 eV) than the other samples. This is in agreement with previous results presented in Table 4.1; however, in this case the difference was lower, because the time span between the plasma cleaning and UPS measurement was longer (3 days compared to few hours). This suggests that the plasma cleaning increases the work function only for a short period of time and then it returns to its original value probably also due to adsorption of adventitious contamination.

No trend was observed in the KPFM results probably due to the fact that the measurements were performed after additional 4 days and in ambient conditions.

Fig. 4.12 displays the results of the valence band edge examination by UPS. The $E_F - E_v$ was determined by fitting the linear region of the spectrum in 4.12a. The resultant values displayed in 4.12b are by ∼0.6 eV lower for samples that were plasma treated. However, even if the $E_F - E_v$ is lower, there are some states visible in the spectrum from 2.5 eV binding energy, similar to the untreated samples. Only the density of states may be lower in the 2.5-4.0 eV region since the UPS signal is lower in that region compared to the plasma treated sample.

If we look at the results of XPS measurements on ITO samples (Fig. 4.13), no significant change is observed. Only the amount of carbon at sample ito7 is significantly higher. This is most probably caused by some unintentional external contamination rather than by the sample preparation, because this sample was not even exposed to IPA. When the In 3d peak is examined, there is again significant change observed, as seen in Fig. 4.9. Only the untreated sample exhibits different In 3d peak position, which is probably caused by improper charge compensation. This happens because the C 1s peak of this sample has a different shape, and thus may be composed of different components leading to different peak positions.

The work function and the valence band position of ITO is in agreement with expected values from literature (see also Tab. 4.3). However, depending on the sample treatment and the surface conditions, the work function determined by UPS was in rather wider range of values from ∼4.0 eV to ∼4.8 eV. The plasma treatment increased the work

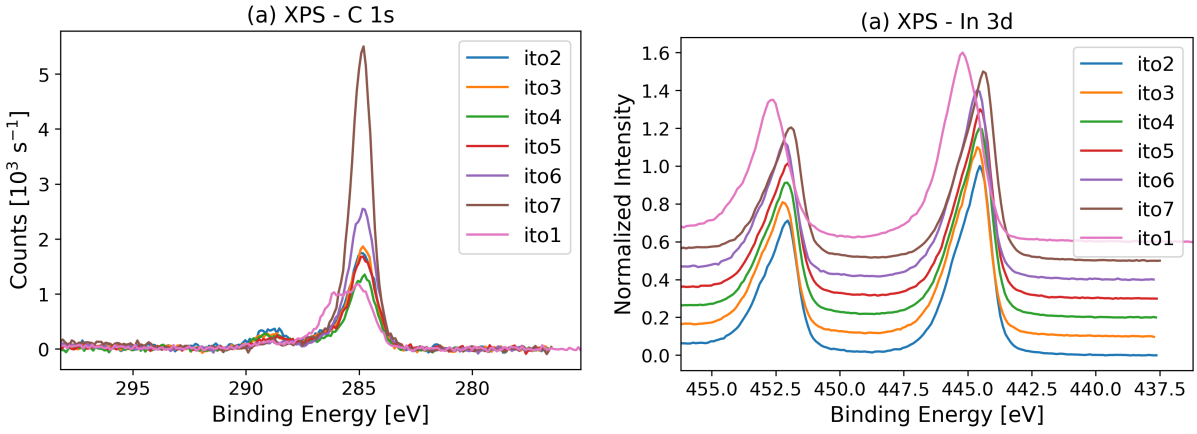

Fig. 4.13: *An XPS comparison of (a) C 1s peak and (b) In 3d peak of all studied ITO samples. No clear relation of chemical composition to the sample preparation was observed. Only the untreated sample (ito1) contamination is composed of different carbon compounds. The C 1s peak is used as charge reference (284.8 eV)*

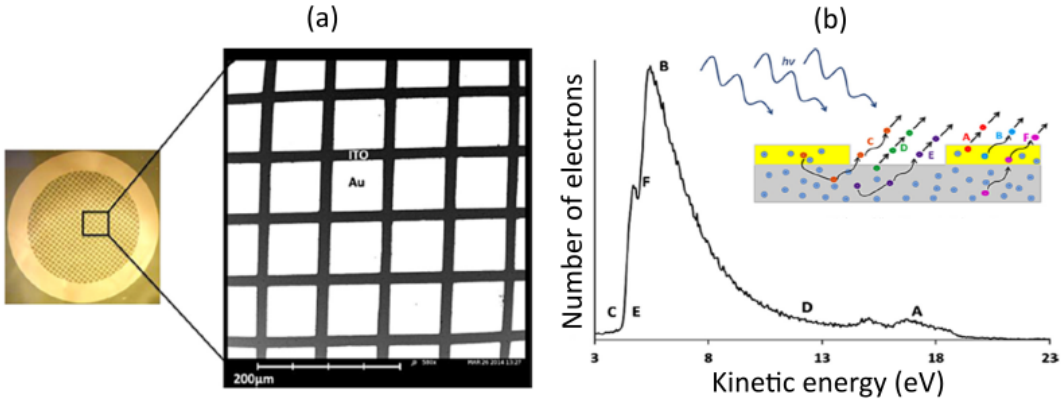

Fig. 4.14: *UPS measurement on a heterogeneous sample by Sharma et. al. (a) Au squares on (white) on an ITO substrate (dark) created by Au deposition through TEM grid. (b) UPS spectrum where two edges (left part) are visible, first corresponds to ITO substrate and the second to the Au squares. Adopted from [70] and edited.*

function even higher (to 5.41 ± 0.07 eV), but only for a short time period. The valence band edge was also different for various treatments (from ∼3 eV for the plasma treated sample to ∼3.5 eV for the untreated samples). No clear correlation between the work functions and the sample treatments was observed when the samples were left in air for a longer period of time (several days). For more information, larger statistical ensemble of measurements would be needed.

The work function of ITO measured by KPFM was generally higher than the one determined by UPS due to the fact that KPFM was measured in ambient conditions. The additional molecules adsorbed on the surface and the humidity changed the work function of both the ITO and the reference value. Therefore, I consider the KPFM measurement to be less reliable.

4.3. Tungsten disulfide nanotubes

In the previous part, measurements of homogenous samples were presented. However, there is one important fact that makes the measurement of tungsten disulfide (WS_2) nanotubes much more difficult. The nanotubes have to be deposited onto some substrate and the signal obtained in the UPS spectrum is an integral signal from a spot of certain size. The spot size depends on the particular instrument, the lens system and its settings. In the settings used during the measurements shown here, the measured spot size was about 1x1 mm (smaller spot size was achievable, but for the cost of the reduction of the signal). Thus, in our case, the spectrum obtained from the UPS measurement is a combination of two spectra – the nanotubes and the substrate. This can make correct evaluation of the work function and the valence band position difficult or even impossible.

It is, however, in some cases possible to extract the work function of both materials, as presented for example by Sharma et al. [70]. They measured UPS on a sample with gold squares deposited onto an ITO substrate, using TEM (Transmission Electron Microscope) grid as a mask. They observed a two high-binding energy edges corresponding to the work function of each material (fig. 4.14).

The idea of analyzing the nanotubes by UPS is following: the nanotubes have to be depositend onto a suitable (conductive) substrate that has significantly different (prefer-

ably higher) work function, which may allow a distinction between the two materials in the spectrum like in the case of Au/ITO structure measured by Sharma et al. (Fig. 4.14). Similarly, in order to extract the valence band edge, a substrate material with wide band gap and Fermi level close to the conduction band may be suitable (because it does not contribute to the spectrum in the low BE region, where signal from WS_2 is expected).

For that reason, Au (100 nm polycrystalline layer on Si) and ITO (few μm layer on a glass substrate, commercially available) were chosen as possibly suitable substrates. They are both cheap, easy accessible and conductive (note that the ITO is an n-doped semiconductor with a band gap in range of 3.5-4.3 eV, E_F close to the conduction band and its conductivity is governed by oxygen vacancies and tin dopant atoms [71]).

Table 4.3: *Expected values of work function ϕ and valence band position with respect to Fermi level $E_F - E_v$.*

Material	ϕ [eV]	$E_F - E_v$ [eV]	note / reference
Au	5.1-5.5	0.0	measured – CPD, PE, FE [72, 73, 74, 75]
ITO	4.4-4.5	-	measured – UPS [76]
ITO	4.5 (6.0)	-	untreated (in situ O_2/Ar plasma cleaned) measured – UPS [69]
ITO	-	3.1-3.2	measured – UPS [77]
WS_2	5.1	-	nanotube, measured [78]
WS_2	-	0.7-0.8	1 layer nanotube, calculated [79]
ITO	4.72 ± 0.7	3.50 ± 0.8	measured – UPS, no treatment [This work]
ITO	3.95 ± 0.7	3.32 ± 0.8	measured – UPS, sputtered [This work]
ITO	5.41 ± 0.7	2.99 ± 0.8	measured – UPS, no treatment [This work]

CPD - Contact Potential Difference, PE - Photoemission, FE - Field Emission

4.3.1. Elimination of surface contamination

Elimination of surface contamination by sample preparation

Any kind of surface contamination is unwanted during the UPS measurements since it can modify the characteristics determined from the spectra. The nanotubes were available in the form of a powder which was dispersed in a solution and drop-casted onto a desired substrate. In order to reduce the effect of the contamination from the solvent, different solvets were tried – isopropyl alcohol (IPA), cyclohexane (C_6H_{12}) and demineralized water. With IPA, it was hard to achieve high coverage with the nanotubes. A mixture of cyclohexane and water (immiscible chemicals) provides a possibility of increasing the coverage. The NTs are dispersed in C_6H_{12} and then water is added. On the C_6H_{12}/water interface, a layer with high density of NTs is formed and when the substrate is dipped into the mixture and removed, the NTs stick on the sample. It is also possible to disperse the NTs in pure water, which was found to be a kind of compromise between high coverage and lower additional carbon contamination.

From Fig. 4.15a one can see that sample with nanotubes dispersed in water exhibits less carbon contamination. However, it was found out that the nanotubes slowly oxidize when dispersed in water for longer time (more than a month) as can be seen in Fig. 4.15b.

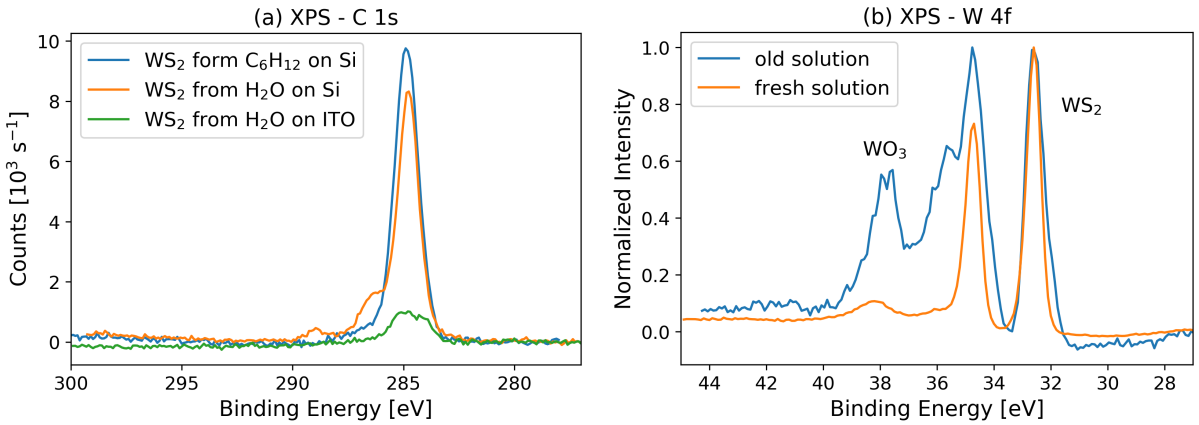

Fig. 4.15: *XPS spectra acquired on various samples with WS_2 nanotubes. (a) C 1s spectra – the amount of carbon contamination is lower when the nanotubes are deposited from water compared to organic solvents. (b) W 4f spectra of samples with nanotubes from water – the peak indicates formation of WO_3 when the nanotubes are kept in aqueous solution for a longer time (∼1 month).*

Elimination of surface contamination by in-situ sputtering

Since there is always an adventitious carbon contamination on the samples as soon as they are exposed to the atmosphere, in-situ sputtering is a common method how the surface can be cleaned for UPS measurements. However, our samples are not flat and homogeneous; therefore, cautious analysis of the effect of sputtering should be done.

First, a sample with WS_2 nanotubes from aqueous solution on Si was in-situ sputtered by $Ar500^+$ ion clusters with energy of 2.5 keV for 120 s. To find out whether the nanotubes are damaged by the sputtering, SEM (Scanning Electron Microscope) image was acquired before and after sputtering (Fig. 4.16). No structural changes were observed after the sputtering. However, carbon contamination was only partially removed.

The reason why the carbon was not completely removed by sputtering might be a "shadowing effect" of the nanotubes. Since the sample is sputtered from an angle of about 45°, the ions might not reach the surface hidden behind the nanotubes. In order to eliminate this effect, the sample was sputtered more times and rotated by 90° between each sputtering cycle. Unfortunately, neither this procedure worked well for complete carbon contamination removal (Fig. 4.17a). Although the rotation of the sample slightly improves the sputtering process, after a few cycles, the sputtering becomes ineffective and some carbon still remains on the sample. Furthermore, as the W 4f peak indicates, subsequent sputtering causes also a removal of tungsten, indicating slight damage to the nanotubes (Fig. 4.17b).

Elimination of surface contamination by annealing

Unfortunately, annealing was found to be an unsuitable method for removing carbon contamination. Although the nanotubes might possibly withstand quite high temperature (they are produced at 850 °C [80]), the substrate choice appeared to be the limiting factor.

When an ITO + WS_2 NTs sample was annealed in vacuum (250 °C, 5h), the amount of carbon was again only partially reduced, and the UPS spectrum measured after anneal-

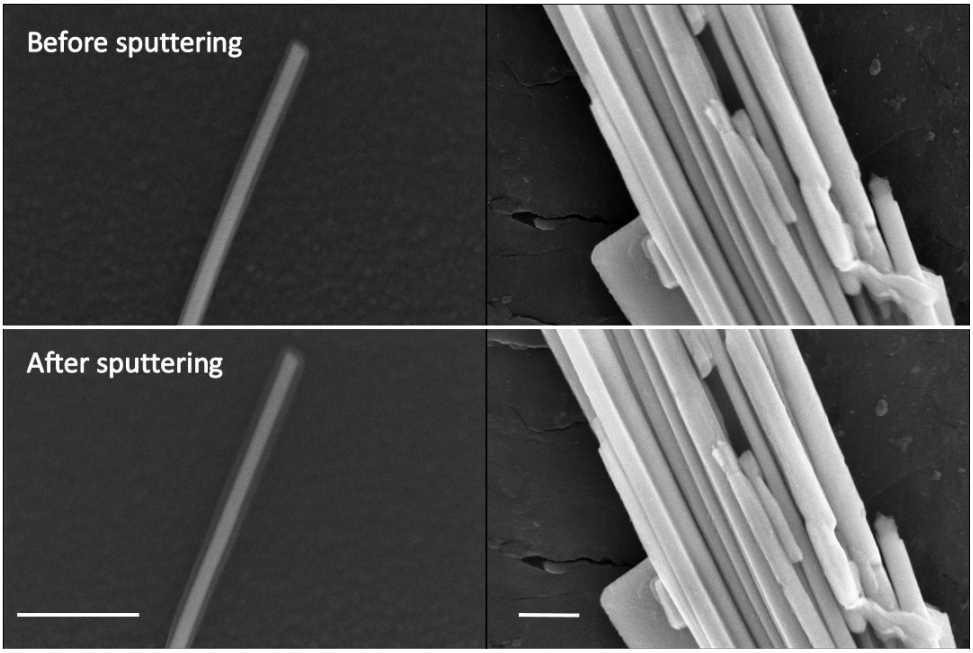

Fig. 4.16: *Effect of sputtering: SEM image of a WS_2 nanotube and a bundle of nanotubes deposited from water onto the same Si sample. Images were acquired before and after sputtering. No structural change is visible after sputtering. The scale bars are is 250 nm.*

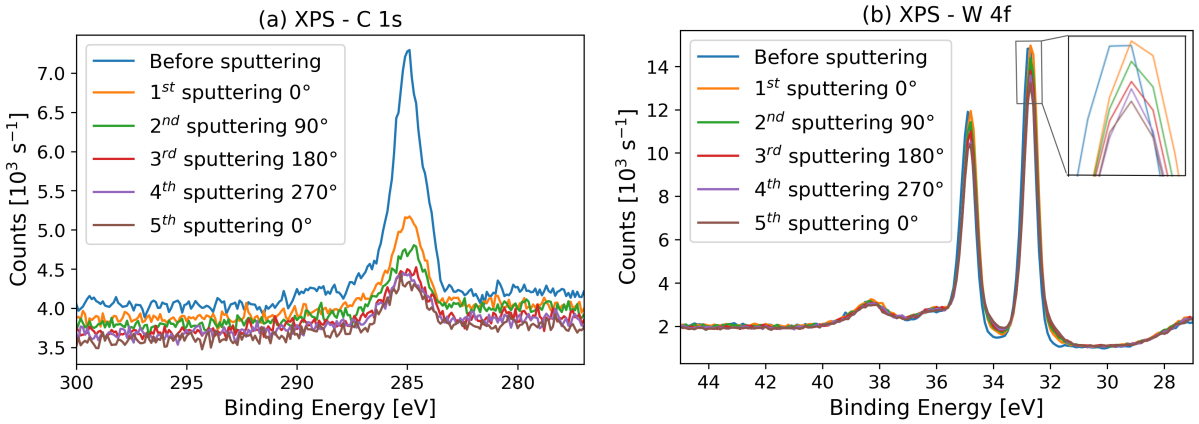

Fig. 4.17: *Effect of sputtering: (a) C 1s and (b) W 4f peak of a sample with WS_2 NTs on ITO after multiple sputtering cycles. The sample was rotated by 90° between each cycle. The complete removal of carbon was not successsful and more, the slight reduction of the W 4f peak indicates also slight damage to the nanotubes during sputtering (the instet in (b)).*

ing was distorted (the "tails" on both sides of the spectrum) as can be seen in Fig. 4.19. Such spectrum is for sure not correct. The reason for this distortion is unknown, but I think it could possibly be explained by a formation of a non-conductive layer on the surface. In order to collect slow electrons, -9 V bias is applied on the sample and if there is a non-conductive layer on the surface, electrons escaping from different depth feel different potenial. Then, the analyzer detects slower electrons than theoretically possible, simply because they were accelerated by a smaller potential difference.

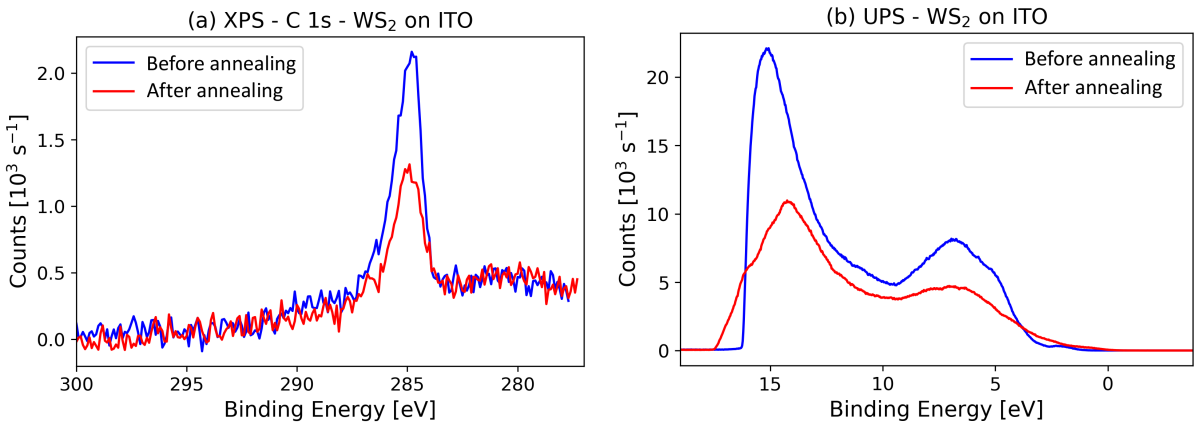

Fig. 4.18: *Effect of 5h 350 °C annealing: (a) Carbon contamination and (b) UPS spectrum. Measured on an ITO substrate with WS_2 NTs. Carbon contamination is only partly reduced and the UPS spectrum is distorted, perhaps due to formation of a nonconductive surface layer.*

Since gold was expected to be a suitable substrate (gold generally exhibited less carbon contamination compared to ITO), it was studied, whether annealing can remove carbon contamination from gold and what temperature can the gold substrate (100 nm Au on Si) withstand. This time, temperature was gradually increased (150 °C, 250 °C, 350 °C, 1 h at each temperature) and XPS was measured at each temperature to detect changes in the surface layer. The Au layer, however, did not survive the 350 °C temperature as the Si substrate started to be visible in the XPS spectrum. The carbon was also not removed effectively.

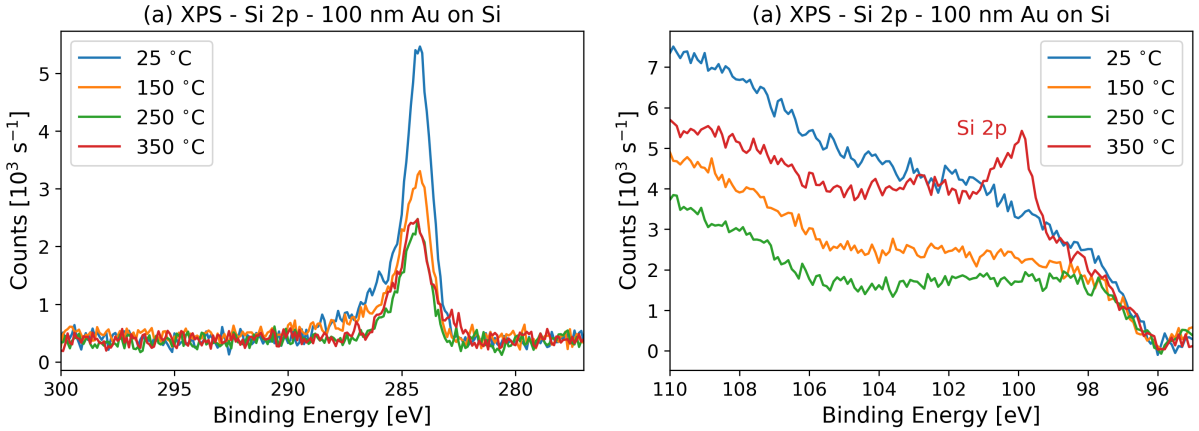

Fig. 4.19: *Effect of annealing on 100 nm Au layer on Si: (a) Carbon contamination was again not removed effectively and (b) the substrate started to be visible in the spectrum.*

4.3.2. UPS results

As described above, complete removal of carbon contamination was not achieved with using any of the presented approaches. However, this fact did not limit the possibility to analyze the valence band edge of the nanotubes. Because neither the ITO nor the ad-

ventitious contamination contribute to the spectrum in the binding energies of ∼0-3 eV, features that belong to the nanotubes can be directly observed. In Fig. 4.20, a comparison of different UPS measurements on ITO substrate with or without WS_2 nanotubes is presented.

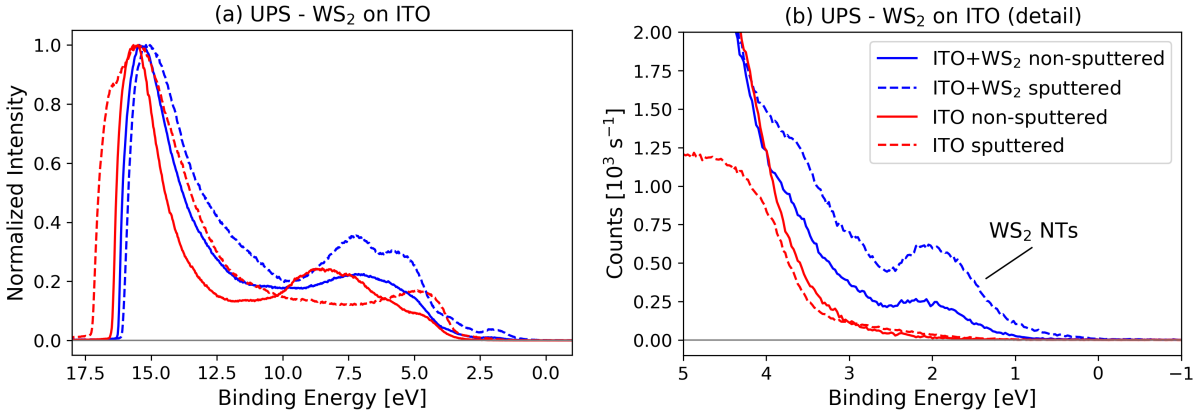

Fig. 4.20: *UPS spectra of plain ITO and ITO with WS_2 NTs. Both samples were measured before and after sputtering. (a) Whole spectrum and (b) detail of the valence band edge. The valence band edge of WS_2 NTs is at ∼1 eV but we can detect also some in-gap states closer to the Fermi level.*

If we look at the detail of the spectrum in Fig. 4.20b, we can see that both sputtered ITO (without carbon) and non-sputtered ITO (with carbon contamination) exhibit very low signal in the region 0-3 eV in binding energy with valence band edge . This was expected for the case of ITO due to its wide band gap and n-type behaviour. Additionally, the carbon contamination rather does not contribute to the spectrum in that region, so we can observe the features in the spectrum arising from WS_2 NTs even if the surface contains carbon contamination. The sputtering causes an increase of the signal from the NTs since more WS_2 surface is expected to be exposed after sputtering. The WS_2 NTs valence band edge was determined to be at 1.07±0.08 eV for the non-sputtered sample and 0.97±0.08 eV for the sputtered sample, which is only slightly higher than the calculated value 0.7-0.8 eV for single wall NTs presented in Table 4.3. However, there are also some in-gap states visible almost up to the Fermi level, probably due to states at the ends of the nanotubes, which are often corrugated.

In the spectrum of WS_2 NTs on Au (Fig. 4.21), it is possible to see the same valence band feature as on the previous spectrum of WS_2 NTs on ITO, confirming that this feature is related to the nanotubes and not to the substrate. The valence band position was, however, not determined from this spectrum, because the position is more hidden in the background arising from the Au. To extract the WS_2 signal, the bare sputtered Au spectrum was subtracted from the sputtered WS_2 + Au spectrum. When compared to the sputtered ITO spectrum, the WS_2 valence band feature appears at the same position for both spectra (Fig. 4.21, note that the subtracted spectrum was scaled for comparison purposes), indicating that there was no shift due to sample charging present (the Au Fermi level works as a reference).

As can be seen in both figures 4.20a and 4.21a, the high-binding energy edge of the spectrum that is used for the work function determination (let's call it "work function edge") appears always at different position. Due to the presence of the carbon contamina-

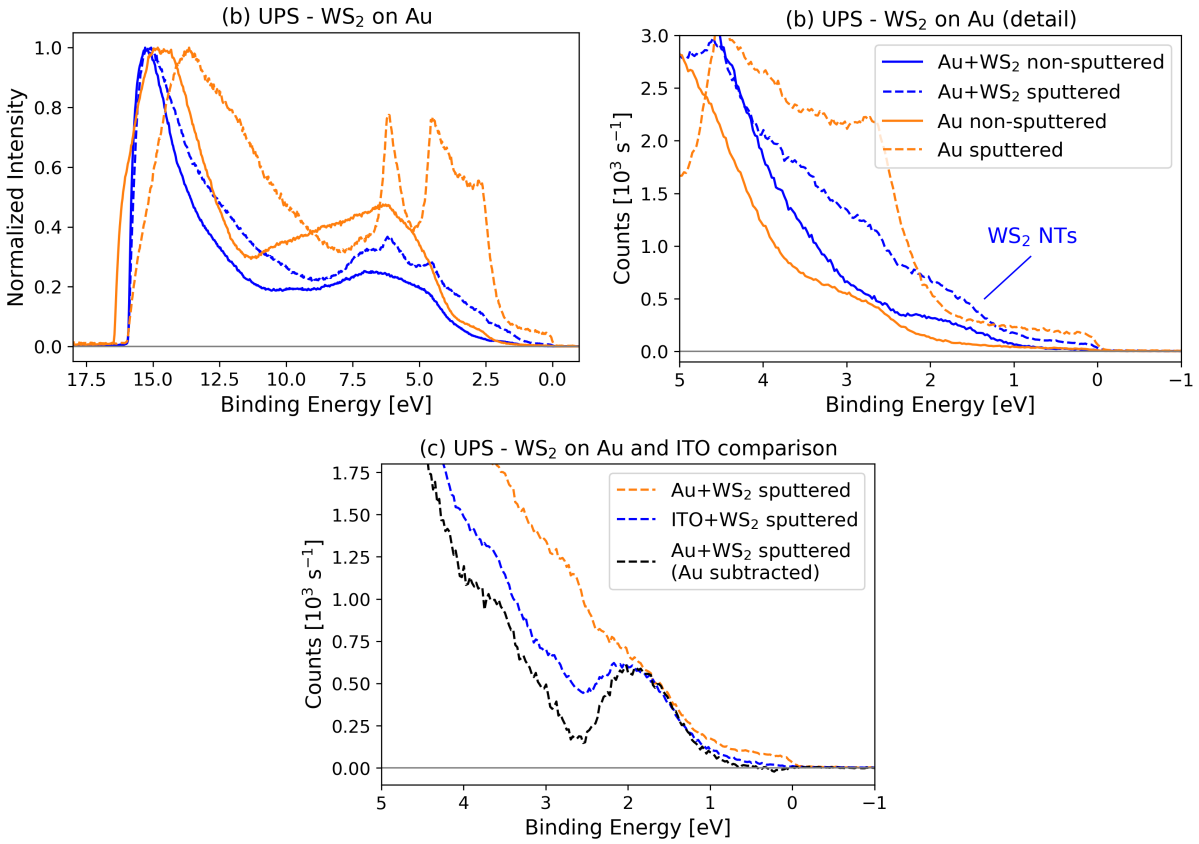

Fig. 4.21: *UPS spectra of plain Au and Au with WS_2 NTs. Both samples were measured before and after sputtering. (a) Whole spectrum and (b) detail of the valence band edge. The valence band edge feature of WS_2 NTs is also visible in the region of 1-2 eV as well as on ITO, but some of the information is hidden in the background from Au. (c) Comparison of WS_2 NTs spectra on Au and ITO. The bare sputtered Au spectrum was subtracted from the sputtered WS_2 + Au spectrum and scaled. The WS_2 valence band feature is almost identical for both substrates.*

tion on the samples with WS_2 NTs, it was not possible to determine whether the signal at the edge comes from the NTs, the substrate or the contamination. Moreover, the slope of the work function edge is sometimes less steep, indicating that there is spread of the work function values, which might be the case of polycrystalline gold, where the work function depends on the crystallographic orientation. Moreover, due to the same reason, the work function of nanotubes measured by UPS might not be correct either because the nanotubes are, first, cylindrical and, second, one is sometimes lying on top of the other. This leads to the fact, that the electrons collected by the analyzer (escaping in the normal direction to the sample) are actually emitted at different angles with respect to the nanotube layers hence the work function can be different. An improvement might be achieved using a well defined substrate. Such substrate can be for example a gold single crystal. However, gold single crystal substrate was not available.

Last, one more approach was tried to remove the carbon contamination. As the plasma cleaning appeared to be the most efficient method of removing organic contamination, a whole sample with WS_2 NTs on ITO was inserted to the plasma cleaner for 1 minute with O_2/Ar plasma. As expected, the nanotubes were oxidized by the plasma as can be seen in Fig. 4.22a. However, the UPS measurement yielded one interesting result. Such

oxidized nanotubes do not have the valence band peak feature in the spectrum so they have much higher $E_F - E_v$ compared to the WS_2 nanotubes (Fig. 4.22b). This also means that the oxidized NTs have higher band gap than 3 eV and probably exhibit n-doped behaviour. This result is consistent with a higher band gap of WO_3 nanowires reported in [81, 82] as ∼3.3-4.0 eV.

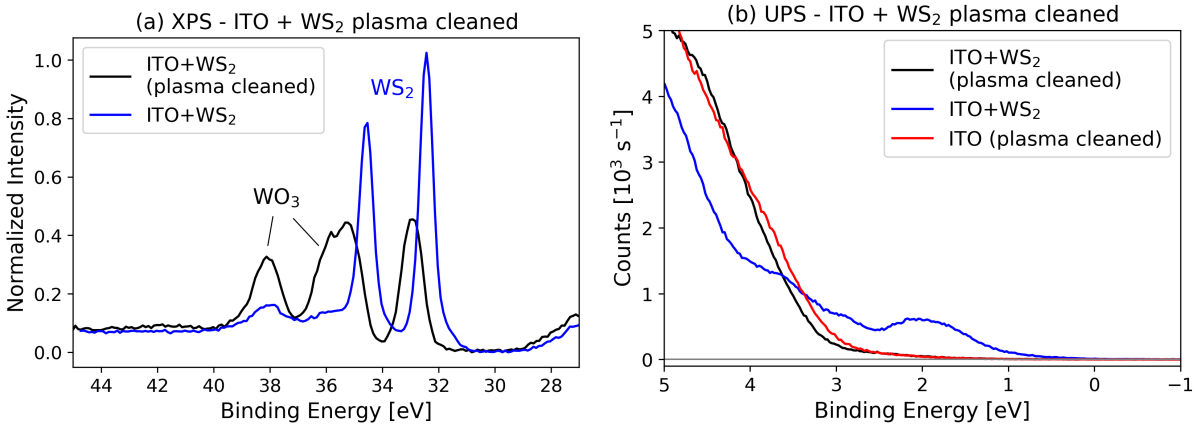

Fig. 4.22: *XPS and UPS measurements of nanotubes oxidized by plasma treatment. (a) XPS: the second peak on the left from the main WS_2 peak indicates formation of WO_3 due to the plasma treatment. The spectra were normalized so the area under both of them is equal to 1. (b) UPS: the valence band feature of WS_2 is not visible in the spectrum of plasma treated sample. This indicates that oxidized nanotubes have much higher $E_F - E_v$.*

Conclusion

Although the thesis title is "Characterization of electronic properties of nanowires for electrochemistry", a broader view on the topic was considered and the analysis was not restricted to "nanowires", but 1D nanostructures in general. The main goal of this thesis was to support electrochemical experiments in dissertation thesis of Ing. Filip Ligmajer, Ph.D. and measure the electronic properties of the electrode materials utilized in his experiments. He used ITO electrodes covered with tungsten disulfide nanotubes. Upon illumination of the electrode, he observed electrochemical changes which were explained with band structure diagrams constructed according to literature values. In this study, the work function and the valence band position with respect to the Fermi level of those materials were analyzed.

As a main tool of analysis, Ultraviolet Photoelectron Spectroscopy was chosen. First, some difficulties related to the UPS measurements were discussed. In particular, the spectrum was shifting after each consecutive measurement. This problem was solved by sputtering the substrate (if possible) or by choosing sufficiently conductive substrate (for the WS_2 nanotubes measurement). It was also noticed, that the ITO UPS spectrum measured on the same spot after XPS analysis was different from the spectrum measured before X-ray irradiation from XPS. This leads to a difference in the work function extracted from the spectra by more than ∼0.5 eV and is attributed to some changes or charging of the surface contaminant layer.

On a sputtered sample, the work function of our ITO substrate was determined as $\phi = 3.95 \pm 0.07$ eV and the valence band position with respect to the Fermi level as $E_F - E_v = 3.32 \pm 0.08$ eV. This should correspond to the pure Sn:In_2O_3 according to XPS results. However, when performing the electrochemical experiments, the ITO is often plasma treated prior to the nanotubes deposition. The ex-situ plasma treated sample showed much higher work function of $\phi = 5.41 \pm 0.07$ eV but slightly lower $E_F - E_v = 3.32 \pm 0.08$ eV. This work function increase was also reported in the literature, where even higher work function of ∼6 eV was obtained after in-situ plasma treatment. The increased work function, however, gradually returns back to the value of ∼4.4-4.6 eV as measured on an untreated sample or several days after plasma treatment (Tab. 4.1 and Fig. 4.11), which may be assigned to a gradual increase of adsorbate coverage.

During the attempts to analyze the WS_2 nanotubes it was noticed that on a sample where the nanotubes were deposited from water, a significantly different In 3d peak was observed in XPS (Fig. 4.9). The explanation was a possible formation of InOOH/$In(OH)_3$ compounds at the surface since this was observed on a sample that was exposed to water for several hours (the aqueous solution with nanotubes was drying very slowly). However, in following experiments, the same effect was not observed repeatedly. Anyway, such possibility should be considered when performing electrochemical measurements in aqueous or hydroxide solutions.

Because the nanotubes are deposited onto the substrates from a solution (water, IPA, etc.), the impact of the sample pre-treatment and the deposition procedure on the ITO properties was tested. Several test samples were prepared with different treatments and their combinations (plasma, solvent deposition, solvent deposition at elevated temperature). Those samples were subsequently analyzed by UPS and KPFM. To have a reference for the KPFM measurements, a 25 nm gold layer was deposited onto a part of each sample prior to all other treatments. It was, however, difficult to find consistent correlation

between the measured work function and the treatment. Only the plasma treatment had stable noticeable effect. The work function of plasma treated samples was by ∼0.1-0.2 eV higher and the $E_F - E_v$ determined by linear fit was by ∼0.6 eV lower (Fig. 4.11 and 4.12).

When it comes to the analysis of WS_2 nanotubes, a suitable substrate has to be chosen. Two different substrates were selected – Au and ITO due to their conductivity and suitable band structure. Moreover, Au is not reactive, and ITO is the same material as was used in the electrochemical experiments. Unfortunately, the work function of WS_2 nanotubes was not measured. One of the main problems was that UPS is very surface sensitive and sufficient removal of adventitious carbon contamination was not achieved. To initially avoid additional carbon contamination, the nanotubes were deposited from water instead of organic solvents (Fig. 4.15). In order to further remove the contamination, sputtering, annealing and plasma cleaning were tried. The sputtering was not successful probably due to shadowing effect of the nanotubes. Even when the sample was sputtered more times and rotated by 90° between each sputtering cycle, carbon contamination was only partially removed (Fig. 4.17a). Moreover, the nanotubes were probably slightly damaged, since a reduction in W and S peak intensity was observed in the XPS spectrum (Fig. 4.17b). The annealing failed due to instability of the substrate at temperatures necessary for removing the contamination (Fig. 4.19, 4.19). Plasma cleaning has proven to be the most effective way of removing carbon contamination (Fig. 4.8a); however, it also caused an oxidation of the nanotubes (Fig. 4.22).

Better results were obtained from the measurement of the valence band edge position of the WS_2 nanotubes. It turned out that the adventitious contamination does not hinder the determination of this value. This is because the contamination does not contribute to the critical part of the spectrum where this information can be read out. The valence band edge was determined to be at binding energy of 0.97±0.08 eV; however, some in-gap states closer to the Fermi level were also detected. Those states probably arise from defect and surface states at the ends of the nanotube, which are often corrugated.

The measurements of the ITO properties and of the WS_2 nanotubes valence band edge position were successful. The failure in determination of the work function of nanotubes may have two reasons. First, sufficient removal of adventitious carbon contamination was not achieved. Because of that, too many factors contributed to the edge of the spectrum which is used for the work function determination. Therefore, it was not possible to distinguish whether the measured value comes from the nanoubes, the substrate or the contamination. Another reason may be that the work function of both substrates was not well defined. A possible way how this could be overcome is using substrate with a well defined work function, eg. single crystal gold (which is unfortunately quite expensive).

Apart from the above mentioned, there may be still one more fundamental obstacle. It is known that the work function depends on crystallographic orientation. Given that the nanotubes have a cylindrical shape, the photoelectrons coming to the analyzer in direction normal to the surface are emitted under different angles with respect to the nanotube layers. Because of that, the edge in the spectrum assigned to the work function may also be poorly defined. Moreover, there is also a strain in the nanotube layers caused by their curvature. This strain causes a change in the material band structure and is expected to be different for nanotubes with different sizes and number of layers. The issue of determining the work function of nanotubes is therefore more complex than expected and definitely deserves further detailed investigation.

Bibliography

[1] LIANG, J.; ZHENG, Y.; LIU, Z.: Nanowire-based Cu electrode as electrochemical sensor for detection of nitrate in water. *Sensors and Actuators B: Chemical*, vol. 232, 2016: p. 336 – 344, ISSN 0925-4005.

[2] XU, K.; WANG, F.; WANG, Z.; et al.: Component-Controllable $WS2_{(1-x)}Se_{2x}$ Nanotubes for Efficient Hydrogen Evolution Reaction. *ACS Nano*, vol. 8, 8, 2014: p. 8468 – 8476, ISSN 1936-0851.

[3] LIGMAJER, F.: *Advanced plasmonic materials for metasurfaces and photochemistry*. PhD Thesis, Brno University of Technology, Faculty of Mechanical Engineering, 2018.

[4] KLOUDA, P.: *Moderní analytické metody*. Tiskárna Harok, Šenov, 2. ed., 2003.

[5] CHEN, X.; WONG, C. K.; YUAN, C. A.; et al.: Nanowire-based gas sensors. *Sensors and Actuators B: Chemical*, vol. 177, 2013: p. 178 – 195, ISSN 0925-4005.

[6] RAGMIR, N. S.; YANG, Y.; ZACHARIAS, M.: Nanowire-based sensors. *Small*, vol. 6, 16, 2010: p. 1705 – 1722, ISSN 1613-6829.

[7] FAN, Z.; RUEBUSCH, D. J.; RATHORE, A. A.; et al.: Challenges and prospects of nanopillar-based solar cells. *Nano Research*, vol. 2, 11, 2009: p. 829 – 843, ISSN 1998-0000.

[8] APPENZELLER, J.; KNOCH, J.; BJORK, M. T.; et al.: Toward nanowire electronics. *IEEE Transactions on Electron Devices*, vol. 55, 11, 2008: p. 2827 – 2845, ISSN 0018-9383.

[9] ZHANG, C.; WANG, S.; YANG, L.; et al.: High-performance photodetectors for visible and near-infrared lights based on individual WS2 nanotubes. *Applied Physics Letters*, vol. 100, 24, 2012: p. 243101, ISSN 0003-6951.

[10] VASHIST, S. K.; ZHENG, D.; AL-RUBEAAN, K.; et al.: Advances in carbon nanotube based electrochemical sensors for bioanalytical applications. *Biotechnology Advances*, vol. 29, 2, 2011: p. 169 – 188, ISSN 0734-9750.

[11] Li, Y.; Qian, F.; Xiang, J.; et al.: Nanowire electronic and optoelectronic devices. *Materials Today*, vol. 9, 10, 2006: p. 18 – 27, ISSN 1369-7021.

[12] DAI, L.; SOW, C.; LIM, C.; et al.: Metal oxide nanowires – Structural and mechanical properties. *Intech Open* [online]. Intech Open Ltd., London, 2011 [cited2.5.2019], available at: https://www.intechopen.com/books/nanowires-fundamental-research/metal-oxide-nanowires-structural-and-mechanical-properties.

[13] ZHANG, D.; EATON, S. W.; YU, Y.; et al.: Solution-Phase Synthesis of Cesium Lead Halide Perovskite Nanowires. *Journal of the American Chemical Society*, vol. 137, 29, 2015: p. 9230 – 9233, ISSN 0002-7863.

[14] HILL, D. J.; CAHOON, J. F.: Nanowire Synthesis: From Top-Down to Bottom-Up. *Material Matters*, 12.1, 2017 [online, cited 2.5.2019]. Available at: https://www.sigmaaldrich.com/technical-documents/articles/material-matters/nanowire-synthesis.html.

[15] IIJIMA, S.: Helical microtubules of graphitic carbon. *Nature*, vol. 354, 6348, 1991: p. 56 – 58, ISSN 1476-4687.

[16] MONTHIOUX, M.; KUZNETSOV, V. L.: Who should be given the credit for the discovery of carbon nanotubes? *Carbon*, vol. 44, 9, 2006: p. 1621 – 1623, ISSN 0008-6223.

[17] SERRA, M.; ARENAL, R.; TENNE, R.: An overview of the recent advances in inorganic nanotubes. *Nanoscale*, vol. 11, 2019: p. 8073 – 8090, ISSN 2040-3372.

[18] TENNE, R.: *Prof. Reshef Tenne – Early years of research* [online]. Weizmann institute of science. [Cit. 23.4.2017], available at: https://www.weizmann.ac.il/materials/tenne/early-years-research.

[19] KITTEL, C.: *Úvod do fyziky pevných látek*. Praha: Academia, 1. ed., 1985.

[20] NobelPrize.org, *J.J. Thomson – Facts* [online]. Nobel Media AB 2019 [cited 4.4.2019], available at: https://www.nobelprize.org/prizes/physics/1906/thomson/facts/.

[21] RUTHERFORD, E.: LXXIX. The scattering of α and β particles by matter and the structure of the atom. *The London, Edinburgh, and Dublin Philosophical Magazine and Journal of Science*, vol. 21, 125, 1911: p. 669 – 688, ISSN 1941-5982.

[22] BOHR, N.: I. On the constitution of atoms and molecules. *The London, Edinburgh, and Dublin Philosophical Magazine and Journal of Science*, vol. 26, 151, 1913: p. 1 – 25, ISSN 1941-5982.

[23] HOLGATE, S. A.: *Understanding Solid State Physics*. Taylor & Francis, 2010.

[24] Wikipedia.org, *Atomic orbital* [online]. Wikipedia, The Free Encyclopedia [cited 22.4.2019], available at: https://en.wikipedia.org/wiki/Atomic_orbital.

[25] LEACH, A. R.: *Molecular Modeling, Principles and Applications*. Pearson Education Ltd., 2. ed., 2001.

[26] PROCHÁZKA, V.: *Fyzika pevných látek – studijní modul*. Univerzita Palackého, Olomouc, 1. ed., 2012.

[27] IBACH, H.; LÜTH, H.: *Solid State Physics*. Springer-Verlag Berlin Heidelberg, 4. ed., 2009.

[28] TAUC, J.; GRIGOROVICI, R.; VANCU, A.: Optical Properties and Electronic Structure of Amorphous Germanium. *Physica Status Solidi (b)*, vol. 15, 2, 1966: p. 627 – 637, ISSN 1521-3951.

[29] SZE, S. M.; NG, K. K.: *Physics of semiconductor devices*. John Wiley & sons, 3. ed., 2006.

[30] SOMOGYI, K.: A method for the determination of the band gap from hall data. *Physica status solidi (a)*, vol. 15, 1, 1973: p. 199 – 205, ISSN 1862-6319.

[31] FRIEDL, R.: Enhancing the accuracy of the Fowler method for monitoring non-constant work functions. *Review of Scientific Instruments*, vol. 87, 4, 2016: p. 043901, ISSN 1089-7623.

[32] HÜFNER, S.: *Photoelectron Spectroscopy: Principles and Applications*. Springer-Verlag Berlin Heidelberg GmbH, 2003.

[33] WIESENDANGER, R.: *Scanning probe microscopy and spectroscopy: Methods and applications*. Cambridge University Press, 1994.

[34] Encyclopaedia Britannica, *Photoelectric effect* [online]. Encyclopaedia Britannica, inc. [cited 12.3.2019], available at: https://www.britannica.com/science/photoelectric-effect.

[35] ČECHAL, J.: *Analýza povrchů a tenkých vrstev využitím fotoelektronové spektroskopie*. PhD Thesis, Brno University of Technology, Faculty of Mechanical Engineering, 2006.

[36] SEAH, M. P.; DENCH, W. A.: Quantitative electron spectroscopy of surfaces: A standard data base for electron inelastic mean free paths in solids. *Surface and Interface Analysis*, vol. 1, 1, 1979: p. 2 – 11, ISSN 1096-9918.

[37] BARIO, L.; VARGAS, G.: *Photoelectron spectroscopy for surface analysis: X-ray and UV excitation*. Universitat de Barcelona: Handbook of instrumental techniques from CCiTUB. Unitat d'Anàlisi de Superfícies, 2012.

[38] SMITH, G. C.: Quantification of Data from Homogeneous Materials. In:. *Surface Analysis by Electron Spectroscopy: Measurement and Interpretation*, 1994: p. 53 – 73.

[39] SHERWOOD, P. M. A.: In *The Handbook of Surface Imaging and Visualisation*. ed. by HUBBARD A. T., Bocaraton, London CRC Press, London, 1995.

[40] BRIGGS, D.; P., S. M.: Auger and X-ray Photoelectron Spectroscopy. In:. *Practical Surface Analysis*, 1993.

[41] SPECS, *X-ray Monochromator FOCUS 500* [online product file]. Specs GmbH, Berlin, Germany [cited 7.5.2019], available at: http://www.tokyoinst.co.jp/product_file/file/SPC03_cat02_ja.pdf.

[42] Casa XPS, *XPS Instrumentation* [online]. Casa Software Ltd. [cited 12.3.2019], available at: http://www.casaxps.com/help_manual/XPSInformation/XPSInstr.htm.

[43] MOULDER, J. F.; STICKLE, W. F.; SOBOL, P. E.; et al.: *Handbook of X-ray Photoelectron Spectroscopy*. USA: Physical Electronics Division, Perkin-Elmer Corporation, 1992.

[44] SADEWASSER, S.; GLATZEL, T.: *Kelvin probe force microscopy*. New York: Springer-Verlag, 1. ed., 2012.

[45] BINNIG, G.; QUATE, C. F.; GERBER, C.: Atomic force microscope. *Physical Review Letters*, vol. 56, Mar 1986: p. 930 – 933, ISSN 0031-9007.

[46] AVILA, A.; BHUSHAN, B.: Electrical Measurement Techniques in Atomic Force Microscopy. *Critical Reviews in Solid State and Materials Sciences*, vol. 35, 1, 2010: p. 38 – 51, ISSN 1040-8436.

[47] MIRONOV, V. L.: *Fundamentals of scanning probe microscopy*. Nizhniy Novgorod: The Russian Academy of Sciences, 1. ed., 2004, 97 p.

[48] GIESSIBL, F. J.: AFM's path to atomic resolution. *Materials Today*, vol. 8, 5, 2005: p. 32 – 41, ISSN 1369-7021.

[49] MELITZ, W.; SHEN, J.; KUMMEL, A. C.; et al.: Kelvin probe force microscopy and its application. *Surface Science Reports*, vol. 66, 1, 2011: p. 1 – 27, ISSN 0167-5729.

[50] SADEWASSER, S.; LUX-STEINER, M. C.: Correct height measurement in noncontact atomic force microscopy. *Physical Review Letters*, vol. 91, 2003: p. 266101, ISSN 0031-9007.

[51] KOVAŘÍK, M.: *Analysis of one-dimensional structures using Kelvin Probe Force Microscopy*. Bachelor Thesis, Brno University of Technology, Faculty of Mechanical Engineering, 2017, available also at: https://www.vutbr.cz/studenti/zav-prace/detail/101372.

[52] HALPERN, E.; ELIAS, G.; KRETININ, A. V.; et al.: Direct measurement of surface states density and energy distribution in individual InAs nanowires. *Applied Physics Letters*, vol. 100, 26, 2012: p. 262105, ISSN 0003-6951.

[53] KOREN, E.; ROSENWAKS, Y.; ALLEN, J. E.; et al.: Nonuniform doping distribution along silicon nanowires measured by Kelvin probe force microscopy and scanning photocurrent microscopy. *Applied Physics Letters*, vol. 95, 9, 2009: p. 092105, ISSN 0003-6951.

[54] KOREN, E.; BERKOVITCH, N.; ROSENWAKS, Y.: Measurement of Active Dopant Distribution and Diffusion in Individual Silicon Nanowires. *Nano Letters*, vol. 10, 4, 2010: p. 1163 – 1167, ISSN 1530-6984.

[55] KOREN, E.; ELIAS, G.; BOAG, A.; et al.: Direct Measurement of Individual Deep Traps in Single Silicon Nanowires. *Nano Letters*, vol. 11, 6, 2011: p. 2499 – 2502, ISSN 1530-6984.

[56] KRONIK, L.; SHAPIRA, Y.: Surface photovoltage phenomena: theory, experiment, and applications. *Surface Science Reports*, vol. 37, 1, 1999: p. 1 – 206, ISSN 0167-5729.

[57] TAKIHARA, M.; TAKAHASHI, T.; UJIHARA, T.: Minority carrier lifetime in polycrystalline silicon solar cells studied by photoassisted Kelvin probe force microscopy. *Applied Physics Letters*, vol. 93, 2, 2008: p. 021902, ISSN 0003-6951.

[58] SCHUMACHER, Z.; MIYHARA, Y.; SPIELHOFER, A.; et al.: Measurement of Surface Photovoltage by Atomic Force Microscopy under Pulsed Illumination. *Physical Review Applied*, vol. 5, 2016: p. 044018, ISSN 2331-7019.

[59] GIRIDHARAGOPAL, R.; PRECHT, J. T.; JARIWALA, S.; et al.: Time-Resolved Electrical Scanning Probe Microscopy of Layered Perovskites Reveals Spatial Variations in Photoinduced Ionic and Electronic Carrier Motion. *ACS Nano*, vol. 13, 3, 2019: p. 2812 – 2821, ISSN 1936-0851.

[60] LIU, L.; LI, G.: Electrical characterization of single-walled carbon nanotubes in organic solar cells by Kelvin probe force microscopy. *Applied Physics Letters*, vol. 96, 8, 2010: p. 083302, ISSN 0003-6951.

[61] LAN, F.; LI, G.: Direct Observation of Hole Transfer from Semiconducting Polymer to Carbon Nanotubes. *Nano Letters*, vol. 13, 5, 2013: p. 2086 – 2091, ISSN 1530-6984.

[62] LIN, J.; LIU, Y.; LIU, Y.; et al.: SnS2 Nanosheets/H-TiO2 Nanotube Arrays as a Type II Heterojunctioned Photoanode for Photoelectrochemical Water Splitting. *ChemSusChem*, vol. 12, 5, 2019: p. 961 – 967, ISSN 1864-564X.

[63] GELDERMAN, K.; LEE, L.; DONNE, S. W.: Flat-Band Potential of a Semiconductor: Using the Mott–Schottky Equation. *Journal of Chemical Education*, vol. 84, 4, 2007: p. 685 – 688, ISSN 1938-1328.

[64] LIU, C.; HWANG, Y. J.; JEONG, H. E.; et al.: Light-Induced Charge Transport within a Single Asymmetric Nanowire. *Nano Letters*, vol. 11, 9, 2011: p. 3755 – 3758, ISSN 1530-6984.

[65] YOO, H.; BAE, C.; YANG, Y.; et al.: Spatial Charge Separation in Asymmetric Structure of Au Nanoparticle on TiO2 Nanotube by Light-Induced Surface Potential Imaging. *Nano Letters*, vol. 14, 8, 2014: p. 4413 – 4417, ISSN 1530-6984.

[66] PRASHANTHI, K.; Gaikwad, R.; Thundat, T.: Surface dominant photoresponse of multiferroic BiFeO3nanowires under sub-bandgap illumination. *Nanotechnology*, vol. 24, 50, 2013: p. 505710, ISSN 1361-6528.

[67] LI, D.-B.; SUN, X.-J.; JIA, Y.-P.; et al.: Direct observation of localized surface plasmon field enhancement by Kelvin probe force microscopy. *Light: Science & Applications*, vol. 6, 2017: p. e17038, ISSN 2047-7538.

[68] DONLEY, C.; DUNPHY, D.; PAINE, D.; et al.: Characterization of Indium−Tin Oxide Interfaces Using X-ray Photoelectron Spectroscopy and Redox Processes of a Chemisorbed Probe Molecule: Effect of Surface Pretreatment Conditions. *Langmuir*, vol. 18, 2, 2002: p. 450 – 457, ISSN 1520-5827.

[69] ISHII, M.; MORI, T.; FUJIKAWA, H.; et al.: Improvement of organic electroluminescent device performance by in situ plasma treatment of indium–tin-oxide surface. *Journal of Luminescence*, vol. 87-89, 2000: p. 1165 – 1167, ISSN 0022-2313.

[70] SHARMA, A.; BERGER, R.; LEWIS, D. A.; et al.: Invisible high workfunction materials on heterogeneous surfaces. *Applied Surface Science*, vol. 327, 2015: p. 22 – 26, ISSN 0169-4332.

[71] KIM, H.; GILMORE, C. M.; PIQUÉ, A.; et al.: Electrical, optical, and structural properties of indium–tin–oxide thin films for organic light-emitting devices. *Journal of Applied Physics*, vol. 86, 11, 1999: p. 6451 – 6461, ISSN 1089-7550.

[72] RIVIÈRE, J. C.: THE WORK FUNCTION OF GOLD. *Applied Physics Letters*, vol. 8, 7, 1966: p. 172 – 172, ISSN 0003-6951.

[73] UDA, M.; NAKAMURA, A.; YAMAMOTO, T.; et al.: Work function of polycrystalline Ag, Au and Al. *Journal of Electron Spectroscopy and Related Phenomena*, vol. 88-91, 1998: p. 643 – 648, ISSN 0368-2048.

[74] HOLSCHER, A.: A field emission retarding potential method for measuring work functions. *Surface Science*, vol. 4, 1, 1966: p. 89 – 102, ISSN 0039-6028.

[75] HypherPhysics, *Work Functions for Photoelectric Effect* [online]. C.R. NAVE, Georgia State University, 2017 [cited 12.5.2019], available at: http://hyperphysics.phy-astr.gsu.edu/hbase/Tables/photoelec.html.

[76] PARK, Y.; CHOONG, V.; GAO, Y.; et al.: Work function of indium tin oxide transparent conductor measured by photoelectron spectroscopy. *Applied Physics Letters*, vol. 68, 19, 1996: p. 2699 – 2701, ISSN 0003-6951.

[77] LIU, T.; ZHANG, X.; ZHANG, J.; et al.: Interface Study of ITO/ZnO and ITO/SnO2 Complex Transparent Conductive Layers and Their Effect on CdTe Solar Cells. *International Journal of Photoenergy*, vol. Article ID 765938, 2013: p. 8, ISSN 1687-529X.

[78] VOLDMAN, A.; ZBAIDA, D.; COHEN, H.; et al.: A Nanocomposite of Polyaniline/Inorganic Nanotubes. *Macromolecular Chemistry and Physics*, vol. 214, 18, 2013: p. 2007 – 2015, ISSN 1521-3935.

[79] SEIFERT, G.; TERRONES, H.; TERRONES, M.; et al.: On the electronic structure of WS2 nanotubes. *Solid State Communications*, vol. 114, 5, 2000: p. 245 – 248, ISSN 0038-1098.

[80] ROTHSHCHILD, A.; SLOAN, J.; TENNE, R.: Growth of WS2 Nanotubes Phases. *Journal of the American Chemical Society*, vol. 122, 21, 2000: p. 5169 – 5179, ISSN 0002-7863.

[81] HUANG, K.; ZHANG, Q.; YANG, F.; et al.: Ultraviolet photoconductance of a single hexagonal WO3 nanowire. *Nano Research*, vol. 3, 4, Apr 2010: p. 281 – 287, ISSN 1998-0000.

[82] SZABÓ, M.; PUSZTAI, P.; LEINO, A.-R.; et al.: Synthesis and characterization of WO3 nanowires and metal nanoparticle-WO3 nanowire composites. *Journal of Molecular Structure*, vol. 1044, 2013: p. 99 – 103, ISSN 0022-2860.

List of abbreviations

AFM	*Atomic Force Microscopy*
AM	*Amplitude Modulation*
BE	*Binding Energy*
CEITEC	*Central European Institute of Technology*
C-AFM	*Conductive AFM*
CPD	*Contact Potential Difference*
DFT	*Density Functional Theory*
FET	*Field Effect Transistor*
HOMO	*Highest Occupied Molecular Orbital*
IPA	*Isopropyl Alcohol*
ITO	*Indium Tin Oxide*
KPFM	*Kelvin Probe Force Microscopy*
LCAO	*Linear Combination of Atomic Orbitals*
LUMO	*Lowest Unoccupied Molecular Orbital*
MCP	*Multi Channel Plate (detector)*
MFM	*Magnetic Force Microscopy*
NT	*Nanotube*
NW	*Nanowire*
PES	*Photoelectron Spectroscopy*
SEM	*Scanning Electron Microscopy*
SPCM	*Scanning Photocurrent Microscopy*
SPM	*Scannig Probe Microscopy*
STS	*Scanning Tunneling Spectroscopy*
TEM	*Transmission Electron Microscopy*
UHV	*Ultra High Vacuum*
UPS	*Ultraviolet Photoelectron Spectroscopy*
XPS	*X-ray Photoelectron Spectroscopy*